# **Evaluation of Boundary Layer and Urban Canopy Parameterizations for Simulating Wind in Miami** during Hurricane Irma (2017)

ERIC A. HENDRICKS, A JASON C. KNIEVEL, A AND DAVID S. NOLAN

<sup>a</sup> National Center for Atmospheric Research, Boulder, Colorado <sup>b</sup> Rosenstiel School of Marine and Atmospheric Science, University of Miami, Miami, Florida

(Manuscript received 26 August 2020, in final form 17 March 2021)

ABSTRACT: The simulated winds within the urban canopy of landfalling tropical cyclones are sensitive to the representation of the planetary boundary and urban canopy layers in numerical weather prediction models. To assess the subgrid-scale parameterizations of these layers, mesoscale model simulations were executed and evaluated against near-surface observations as the outer wind field of Hurricane Irma (2017) interacted with the built-up region from downtown Miami northward to West Palm Beach. Four model simulations were examined, comprising two different planetary boundary layer (PBL) parameterizations (a local closure scheme with turbulent kinetic energy prediction and a nonlocal closure scheme) and two different urban canopy models (UCMs) [a zeroth-order bulk scheme and a multilayer building effect parameterization (BEP) that mimics the three-dimensionality of buildings]. Overall, the simulated urban canopy winds were weakly sensitive to the PBL scheme and strongly sensitive to the UCM. The bulk simulations compared most favorably to an analyzed wind swath in the urban environment, while the BEP simulations had larger negative biases in the same region. There is uncertainty in magnitude of the urban environment biases due to the lack of many urban sheltered measurements in the wind swath analysis. Biases in the rural environment were similar among the bulk and BEP simulations. An improved comparison with the analyzed wind swath in the urban region was obtained by reducing the drag coefficient in BEP in one of the PBL schemes. The usefulness of BEP was demonstrated in its ability to predict realistic heterogeneous near-surface velocity patterns in urban regions.

KEYWORDS: Boundary layer; Tropical cyclones; Atmosphere-land interaction; Model evaluation/performance; Parameterization; Urban meteorology

### 1. Introduction

One of the gravest threats to coastal cities is the eyewall of an intense tropical cyclone (TC) making a direct landfall. While direct wind damage is often a lesser impact than storm surge inundation and/or rainfall-induced flooding, the landfalls of Hurricanes Michael (2018), Andrew (1992) (Powell et al. 1996; Rappaport 1994), and Hugo (1989) (Powell et al. 1991) are cautionary reminders of the catastrophic wind destruction that can occur when intense hurricanes make landfalls near cities. As an example, Hurricane Andrew caused 25 billion dollars of damage and left 250 000 people homeless (Rappaport 1994). While no significant trends since 1900 have been found in landfalling hurricanes in the United States (Klotzbach et al. 2018), inflation-adjusted damage has increased substantially and will continue to increase with population and infrastructure growth on the U.S. East and Gulf Coasts.

Although hurricanes are deep atmospheric vortices with wind fields that extend to near the tropopause, it is the hurricane boundary layer (HBL), or the layer below approximately 2 km, that directly impacts the underlying land during landfalls. In addition to the strong mean winds, coherent structures spanning multiple time and space scales, such as boundary layer roll vortices (Foster 2005; Morrison et al. 2005; Zhang et al. 2008) and small-scale vortices (Willoughby and Black

Corresponding author: Eric A. Hendricks, erichend@ucar.edu

1996; Aberson et al. 2006; Marks et al. 2008; Guimond et al. 2010; Wu et al. 2018; Guimond et al. 2018; Wurman and Kosiba 2018; Fernández-Cabán et al. 2019), are observed and simulated in HBLs. There have been a number of studies that have examined various aspects of the HBL over open water. These studies range from theoretical (Smith 1968; Shapiro 1983; Kepert 2001; Kepert and Wang 2001; Smith 2003; Ingel 2005; Nolan 2005; Smith and Mongtomery 2010; Rotunno and Bryan 2012; Williams et al. 2013; Kepert 2017, 2018) to observational (Barnes and Powell 1995; Kepert 2006a,b; Drennan et al. 2007; French et al. 2007; Lorsolo et al. 2008; Zhang et al. 2009; J. A. Zhang et al. 2011; Zhang and Drennan 2012; Zhang et al. 2013, 2015) to numerical modeling (Braun and Tao 2000; Nolan et al. 2009a,b; Bryan 2012; Abarca et al. 2015; Smith and Mongtomery 2014b; Kepert et al. 2016; Bu et al. 2017). Significant progress has been made through the above studies and other studies, but the HBL remains an area of keen scientific interest because of its inherent complexity; strong relationship to hurricane structure, intensity, and intensification rate; and its threat to populations and infrastructure during landfalls.

Compared to the many studies of the HBL over open water, fewer studies have examined the HBL as it interacts with land. Zhu (2008) found that Hurricane Wilma's (2005) overall storm intensity decreased with increasing surface roughness over land. However, no corresponding decrease was found in reducing wind gusts, suggesting that wind damage cannot be accurately assessed based on overall storm intensity. Alford et al. (2020) studied the HBL transition across the coastal

interface for Hurricane Irene (2011), and found that the HBL does not immediately adjust to the enhanced roughness over land, leading to strong onshore winds for a prolonged time period. Ming et al. (2014) found different mixed-layer and inflow depths in convective and postconvective periods as rainbands of Typhoon Morakot (2009) interacted with eastern China. Hirth et al. (2012) documented the development of an internal boundary layer during the landfall of Hurricane Fran (2004) near Cape Canaveral, Florida, and found substantial changes in horizontal wind speed (reduction in excess of 20%) and direction. Nolan et al. (2021a) simulated Hurricane Wilma's landfall in southern Florida and found that the simulated near-surface winds over land could be predicted accurately at fixed locations if the track, intensity, and structure of the storm were simulated accurately. Studies have also performed detailed analysis of small-scale linear coherent structures in landfalling HBLs using Doppler-on-Wheels and Shared Mobile Atmospheric Research and Teaching (SMART) radars (Wurman and Winslow 1998; Lorsolo et al. 2008; Kosiba et al. 2013; Kosiba and Wurman 2014). Because dense urban areas occupy a much smaller percentage of a typical coastline than suburban and rural areas, the eyewall of a hurricane is unlikely to make a direct landfall on a central business district. Nonetheless, because of large population centers in cities and expensive, vulnerable infrastructure, the HBL-city interaction problem is of great societal importance. An HBL interacting with the large roughness elements of a city could create complex wind structures that need to be better understood for hazard mitigation. We are not aware of any studies that have rigorously examined the interaction of landfalling hurricanes with cities, although the studies listed above and others have examined surface roughness and land-use impacts on hurricane winds.

To explicitly resolve the interaction of the HBL with a city, a large-eddy simulation (LES) would be needed with horizontal and vertical grid spacings of O(1) m. However, deterministic prediction at these grid spacings might generally not be that useful because of the stochastic nature of turbulence. Moreover, with current computing power, such simulations would not run quickly enough to be of use to warn the public. While one can imagine ensemble LES in the distant future for tackling the hurricane-city interaction problem explicitly, a cruder approach unfortunately must be undertaken for the foreseeable future. In current numerical weather prediction (NWP) models used to simulate TCs at horizontal grid spacings of O(1) km, the net urban effects on a grid cell must be parameterized since the buildings cannot be explicitly resolved. Additionally, because of the coarser vertical grid spacing, vertical mixing by small eddies must also be parameterized in these models through the use of PBL parameterizations. Because these parameterizations will be necessary for the foreseeable future, it is imperative to continually evaluate and improve them so that they accurately simulate the urban canopy winds during hurricane landfalls.

The purpose of this work is to understand how well PBL and urban canopy parameterizations in the Weather Research and Forecasting (WRF) Model simulate the winds within Miami's urban canopy as the outer wind field of Hurricane Irma (2017)

interacts with the city. The horizontal and vertical resolutions of the mesoscale model simulations are not sufficient to explicitly resolve turbulence. Therefore, we will focus on how well the subgrid-scale urban and PBL parameterizations represent the net effects of this turbulence, or equivalently, the bulk properties of the HBL over the urban environment. Since our emphasis is on the urban canopy parameterizations, much of our analysis will be focused on the flow near the surface where the urban sources exist. While Miami avoided a direct by Irma's eyewall, the onshore 1-min sustained winds to Miami observed at the NOAA National Data Buoy Center (NDBC) Fowey Rocks station (reduced to 10 m above sea level; see section 5c) were greater than tropical-storm force (17.4 m s<sup>-1</sup>) from 0000 UTC 10 September to 0300 UTC 11 September (approximately 27 h). Thus, it is a suitable sustained strongwind case for evaluating the model and parameterizations.

### 2. Hurricane Irma (2017) synoptic history near Florida

Irma was one of the strongest Atlantic hurricanes on record and made seven landfalls in northern Caribbean Islands, Cuba, the Florida Keys, and southwestern Florida (Cangialosi et al. 2018). We focus on the time period after 0000 UTC 9 September while Irma was interacting with Cuba and Florida, and report the National Hurricane Center maximum near-surface sustained winds as a metric for the overall storm intensity. Irma made landfall as a category-5 hurricane in Cayo Romano, Cuba, at 0300 UTC 9 September. Irma moved along the northern coast of Cuba and weakened due to its interaction with land. By 1800 UTC 8 September, Irma was a category-2 storm with maximum sustained winds of 95 kt (49 m s<sup>-1</sup>). Irma then slowed and intensified over the warm Florida Straits on 10 September. Irma made landfall on Cudjoe Key, Florida, at 1300 UTC 10 September as a category-4 hurricane with maximum sustained winds of 115 kt (59 m s<sup>-1</sup>). Irma then weakened due to southwesterly shear and made its final landfall on Marco Island, Florida, at 1930 UTC 10 September with maximum sustained winds of  $100 \,\mathrm{kt}$  (51.4 m s<sup>-1</sup>).

The focus of this study is on the impacts of Irma's outer wind field on Miami. While Miami avoided a direct hit by the eyewall, the impacts were severe. The combination of storm surge and tide produced inundation levels of 4-6 ft (1.2-1.8 m) in southeastern Florida, and 2-4 ft (0.6-1.2 m) in coastal sections of Miami-Dade, Broward, and Palm Beach counties (Cangialosi et al. 2018). Significant flooding also occurred in downtown Miami. Irma's large outer wind field produced local winds in Miami from strong tropical-storm to minimal hurricane force. According to the NHC best track data, at 1800 UTC 10 September (near the time of peak winds in Miami) the northeast quadrant radii of 34-kt (17.5 m s<sup>-1</sup>), 50-kt ( $25.7 \,\mathrm{m \, s^{-1}}$ ), and 64-kt ( $32.9 \,\mathrm{m \, s^{-1}}$ ) winds were 555.6, 240.8, and 129.6 km, respectively. Surface stations in the Miami metropolitan area measured 1-min maximum sustained winds between 50 and 73 kt (26–38 m s<sup>-1</sup>) [Fig. 8 of Cangialosi et al. (2018)]. Peak gusts in the same region ranged from 67 to 95 kt (34-49 m s<sup>-1</sup>) [Fig. 9 of Cangialosi et al. (2018)] (note that gusts and sustained winds are near the surface, but not necessarily precisely at 10 m AGL). The long duration of wind speeds at or exceeding tropical-storm force was an important factor that increased the level of damage.

### 3. Urban canopy and boundary layer parameterizations

There are a number of different PBL parameterizations available in the WRF Model, with varying methods of turbulence closure. One of the more common local closure methods is the 1.5-order scheme with prediction of turbulent kinetic energy (TKE). This scheme accounts for mixing between adjacent vertical layers, with the local eddy viscosity coefficient proportional to the TKE. Some other schemes use nonlocal closure. These schemes include gradient correction terms in the vertical diffusion equation to account for nonlocal mixing from deep eddies. Higher-order turbulence closure schemes exist as well. Similarly, there is a hierarchy of four different UCMs of increasing complexity available. The focus of this paper is on four numerical simulations that employ two PBL schemes and two urban canopy parameterizations. The PBL schemes are the Mellor-Yamada-Janjić (MYJ; Mellor and Yamada 1982; Janjić 1994) and the Yonsei University (YSU; Hong et al. 2006). The urban canopy parameterizations are a simple bulk scheme (hereafter BULK) and the multilayer building effect parameterization (BEP; Martilli et al. 2002). Below we provide details of each of these schemes individually, and how the UCMs interact with the PBL schemes. Broadly speaking, the UCMs provide urban sources to the WRF Model state variables near the surface, and the PBL schemes perform vertical mixing.

The simplest urban parameterization approach is a bulk scheme, in which the aerodynamic roughness is increased along with urban changes to the albedo, heat capacity, and conductivity. This approach is simple and does not increase the run time of a simulation, but it cannot adequately capture important details of urban canopy layer processes. On the other end of the spectrum is the multilayer BEP combined with a building-energy model (BEM) (Salamanca et al. 2011). These two parameterizations in conjunction account for the threedimensionality of buildings in a city, include separate thermal and roughness characteristics of roads, walls, and roofs, and include heat exchanges between the interiors of buildings and the environment. With the improved building representation, BEP has more realistic shadowing and radiation trapping effects than simple urban schemes. BEP also includes a building source term for TKE and reduces the turbulence length scales to account for smaller eddies induced by the interaction of the mean flow with buildings. While BEP+BEM is more sophisticated than BEP alone because the pairing includes heat exchanges from the interiors of buildings, we have elected to only use BEP in this study because our primary interest is on nearsurface winds during hurricane landfalls, for which BEM would have minimal effects. We have verified this by running test cases with BEP and BEP+BEM for the landfall of Hurricane Irma (2017), and the near-surface wind fields are similar.

An advantage of BEP over the simple bulk scheme and single-layer urban canopy model (Kusaka et al. 2001) is that it produces vertically distributed sources on its own urban vertical grid with spacing of 5 m across 18 vertical levels (Martilli et al. 2002). BEP predicts separate skin temperatures for roofs,

walls, and roads, leading to accurate urban sensible heat fluxes (Chen et al. 2011). Similarly, momentum and water vapor mixing ratio sources are produced on these horizontal and vertical surfaces. We focus on details of the urban sources that are most relevant to the winds in the urban environment: the drag force and TKE source. The formula for the vertically distributed building wall drag force is

$$\mathbf{F}_{d,i} = -\rho_i C_d |\mathbf{u}_i|^{\text{ort}} \mathbf{u}_i^{\text{ort}} S_i, \tag{1}$$

wherein  $\mathbf{F}_{d,i}$  is the drag force from vertical surfaces,  $C_d$  is the drag coefficient,  $\rho_i$  is density,  $\mathbf{u}_i^{\text{ort}}$  is the component of the horizontal velocity vector orthogonal to a building wall (each wall is treated separately), and  $S_i$  is the surface area of walls on the BEP ith vertical level (Martilli et al. 2002; Raupach et al. 1991). Thus, near the surface  $S_i$  is larger, resulting in a larger drag force, and  $S_i$  becomes zero above the tallest building, resulting in no drag force. The BEP default value of  $C_d$  is 0.4, based on wind tunnel data for flow around a cubical structure (Raupach et al. 1991). The turbulent momentum flux from horizontal surfaces (roofs and roads) is parameterized based on Louis (1979), and is a function of horizontal wind speed, bulk Richardson number, and surface roughness. The BEP TKE calculation is as follows. According to Eq. (22) of Martilli et al. (2002), BEP calculates a turbulence length scale  $l_b$  associated with buildings that is proportional to the building heights. Then the total turbulence length scale is modified according to Eq. (23) of Martilli et al. (2002):

$$\frac{1}{l} = \frac{1}{l_{\text{old}}} + \frac{1}{l_b},\tag{2}$$

wherein  $l_{\rm old}$  is the turbulence length scale without the effects of buildings and l is the new turbulence length scale including the effects of buildings. Through Eq. (2), l is always less than  $l_{\rm old}$  and thus buildings reduce the overall turbulence length scale. The direct building-induced TKE source term in BEP is

$$F_{e,i} = \rho_i C_d |\mathbf{u}_i^{\text{ort}}|^3 S_i, \tag{3}$$

wherein  $F_{e,i}$  is the TKE source term,  $C_d$  is the drag coefficient,  $\rho_i$  is the density,  $\mathbf{u}_i^{\text{ort}}$  is the component of the horizontal velocity vector orthogonal to a building wall, and  $S_i$  is the surface area of walls at the BEP *i*th vertical level. Thus, building-induced TKE is generated by mean wind forcing on vertical surfaces (TKE from horizontal surfaces based on Monin–Obukhov theory is also applied).

These vertically distributed sources on BEP's urban grid are then interpolated to the mesoscale model's vertical grid at each model physics time step. Thus, provided enough mesoscale model levels are used near the surface, vertically distributed sources can also exist in the mesoscale model. The BEP sources, interpolated to the mesoscale model grid, then force the mesoscale model state variables near the surface. This forcing leads to a direct interaction with the PBL parameterizations, and we now describe some important details of this interaction in both the MYJ and YSU PBL parameterizations.

The YSU PBL scheme is a first-order scheme with nonlocal closure (Hong et al. 2006). The implementations of BEP and

BEP+BEM in the YSU PBL scheme are described by Hendricks et al. (2020). The YSU PBL scheme solves a vertical diffusion equation with eddy viscosity coefficient K. Nonlocal effects are accounted for by a gradient correction term  $\gamma_c$ , and the scheme also includes an asymptotic flux term at the inversion layer  $(w'c')_h(z/h)^3$ , wherein w' is the turbulent variation in the vertical velocity, z is the physical height, c' is the turbulent variation of the prognostic variable, and h is the PBL depth. The BEP and BEP+BEM source terms (interpolated to the mesoscale model grid) S = AC + B represents the forcing tendencies to the prognostic variables from the effects of buildings. The source terms are split between an implicit A and explicit B component in the implicit solver, and are threedimensional arrays in space (functions of height and varying in the horizontal directions). The modified YSU vertical diffusion equation for a prognostic variable C with the inclusion of these BEP and BEP+BEM source terms is

$$\frac{\partial C}{\partial t} = \frac{\partial}{\partial z} \left[ K \left( \frac{\partial C}{\partial z} - \gamma_c \right) - \left( \overline{w'c'} \right)_h \left( \frac{z}{h} \right)^3 \right] + AC + B. \tag{4}$$

The urban source terms are computed through the land surface model's call to the BEP and BEP+BEM subroutines [based upon Martilli et al. (2002) and Salamanca et al. (2010), respectively]. The complete A and B terms consist of both the urban and rural values, with linear weighting between urban and rural areas in the land surface model using the urban fraction f (e.g., for implicit source A,  $A_C = (1-f)A_{C,\text{rur}} + fA_{C,\text{urb}}$ , wherein  $A_{C,\text{rur}}$  is the rural component and  $A_{C,\text{urb}}$  is the urban component of state variable C from BEP or BEP+BEM). Thus A and B have values at every horizontal grid point on at least the first mesoscale model vertical level.

The MYJ PBL scheme is a 1.5-order scheme with local closure. TKE is predicted, and the eddy viscosity coefficient *K* is proportional to the TKE and turbulence length scale. The MYJ PBL parameterization solves a vertical diffusion equation with the same BEP and BEP+BEM source terms:

$$\frac{\partial C}{\partial t} = \frac{\partial}{\partial z} \left( K \frac{\partial C}{\partial z} \right) + AC + B, \tag{5}$$

wherein C is the prognostic variable and A, B are the BEP or BEP+BEM source terms. In both PBL schemes, BEP and BEP+BEM provide net subgrid-scale tendencies for the potential temperature, zonal velocity, meridional velocity, and water vapor mixing ratio (i.e.,  $C = \theta$ , u, v,  $q_v$ ). The main difference between the MYJ and YSU PBL parameterizations is that the vertical diffusivity K is directly modified by TKE produced by buildings in MYJ, whereas in YSU, the amplitude of the vertical profile of K is modified by the changes in the surface fluxes. With the TKE and turbulence length scale modified by the effects of buildings in BEP, the vertical diffusivity K is proportional to l and  $(TKE)^{1/2}$ . The MYJ TKE equation includes advection, shear and buoyancy production terms, building-generated TKE, and a TKE dissipation term. The TKE dissipation term is directly proportional to the TKE and inversely proportional to the total turbulence length scale. The net effect of buildings on local vertical mixing is thus dependent upon the competing factors of TKE production from buildings, and TKE dissipation through the reduction of the total turbulence length scale. Brief descriptions of the numerical solutions to Eqs. (4) and (5) are given in appendix A.

In summary, the MYJ PBL parameterization is similar to the YSU PBL parameterization in that BEP's implicit A and explicit B near-surface source terms directly force the momentum, potential temperature, and water vapor mixing ratio there. The main differences are due to the vertical diffusivities. In the YSU PBL parameterization, the amplitude of the eddy viscosity coefficient profile is modified through the BEP surface fluxes as well as the countergradient correction term  $\gamma_c$ (Hendricks et al. 2020). This is a nonlocal effect whereby mixing in the PBL is directly changed through surface forcing in BEP. In the MYJ PBL parameterization, the vertical diffusivity is modified locally through the TKE budget equation and modified turbulence length scales. Since the mesoscale model simulations are run with a smallest horizontal grid spacing of 0.67 km, the net effects of eddies with scales less than the effective resolution (Skamarock 2004) of approximately 6- $7\Delta x$  (or approximately 4 km) are parameterized, while eddies larger than this grid spacing are explicitly resolved. Similarly, BEP produces a net tendency for all the buildings within a  $0.67 \, \mathrm{km} \times 0.67 \, \mathrm{km}$  grid cell to feed back to the mesoscale model grid-scale variables. As will be discussed, our simulations use 15 vertical levels below 2 km, yielding an average vertical grid spacing of 133 m at lower levels. Vertical mixing by eddies greater than 500 m in the vertical is explicitly resolved while mixing by eddies smaller than this is parameterized through the PBL schemes.

### 4. Description of numerical simulations and observations

# a. Model setup

The WRF Model, version 4.1 (Skamarock et al. 2005), is used for the numerical simulations. Four nested grids, with horizontal grid spacings of 18, 6, 2, and 0.67 km are used, respectively (Fig. 1). The number of horizontal grid points on these grids are  $250 \times 250, 250 \times 250, 400 \times 400, \text{ and } 301 \times 400,$ respectively. There are 60 vertical levels on the WRF Model's stretched grid (with a lowest level of approximately 26.5 m), and 15 levels are below 2 km for high vertical resolution of the PBL. The initial and lateral boundary conditions are from the National Centers for Environmental Prediction Global Data Assimilation System/Final analysis (NCEP GDAS/FNL) at 0.25° horizontal grid spacing. The simulations are initialized at 1200 UTC 9 September 2017 and run until 1200 UTC 11 September 2017. The peak winds in Miami were between 1500 and 1800 UTC 10 September, and the simulations cover all times when the winds exceeded tropical-storm force in Miami. To help constrain the track of Irma to the observations, large-scale nudging is applied on domain 1 to momentum, potential temperature, and water vapor mixing ratio with a relaxation coefficient of  $2.31 \times 10^{-5}$  s<sup>-1</sup> (or a 12-h 1/e-damping time). Vortex bogussing (Kurihara et al. 1993) was not necessary in this study because of the high-resolution analysis and quality of the initial vortex.

Physical parameterizations are the Rapid Radiative Transfer Model (RRTM) shortwave and longwave parameterizations

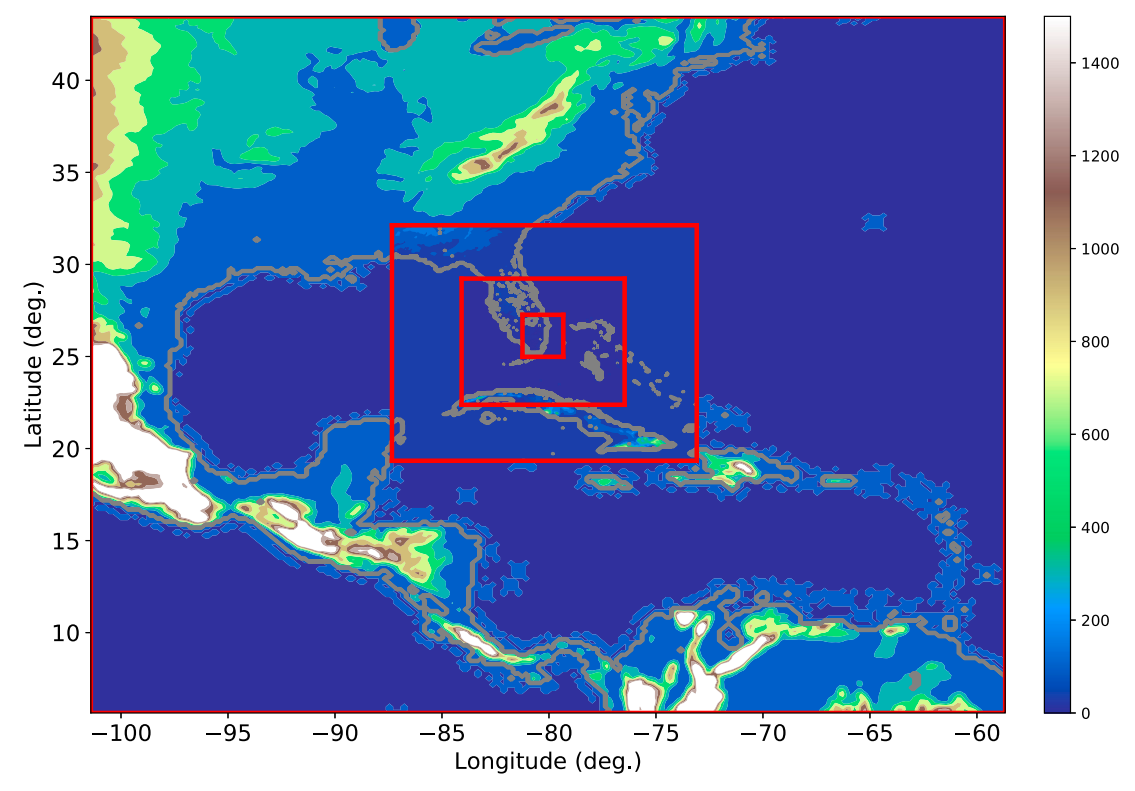


FIG. 1. The four nested WRF Model domains (red outlines) with horizontal grid spacings of  $\Delta x = 18, 6, 2$ , and 0.67 km, from outer to inner. The terrain height (m) at each grid's horizontal resolution is shaded.

(Iacono et al. 2008), the unified Noah land surface model (Ek et al. 2003; Tewari et al. 2004), and the double-moment 5-class microphysical parameterization (Lim and Hong 2010). The new Tiedtke scheme (Tiedtke 1989; C. Zhang et al. 2011) is used on the 18-km grid to include the net effects of subgrid-scale convection, and convection is calculated explicitly through the microphysical equations on the rest of the grids. The simple onedimensional mixed-layer ocean model (Pollard et al. 1972) is used with a mixed-layer depth of 25 m and lapse rate below the mixed layer of 0.14 K m<sup>-1</sup>. The surface bulk drag and enthalpy coefficients are modified to be consistent with laboratory studies in high winds (Donelan et al. 2004; Haus et al. 2010) over water. Over rural land areas, the exchange coefficients are based on the WRF surface layer parameterizations. The eta similarity scheme (Janjić 1994) is used with the MYJ PBL parameterization, while the revised MM5 parameterization (Jiménez et al. 2012) is used with the YSU PBL parameterization. Over urban areas, BEP determines these exchange coefficients. For inspection of how the urban canopy layer and PBL change over time, state variables are written out every 10 min on domains 3 and 4. On domain 4, the diagnosed near-surface winds [10 m above ground level (AGL)], are written out every 20 s in order to compare to observations of 1-min maximum sustained winds.

The building morphology for BEP comes from the National Urban Database and Portal Tool (NUDAPT) (Ching et al. 2009; Chen et al. 2011). These data include urban fraction, impervious fraction, building height histograms, building-plan area fraction, building height weighted by footprint plan area,

and building-surface-area-to-plan-area ratio. NUDAPT grids all building data to a  $1 \text{ km} \times 1 \text{ km}$  horizontal grid. Since each grid cell contains multiple buildings in dense urban areas, these values are representative of the average building characteristics in a grid cell. In addition to the NUDAPT data, BEP requires road, roof, and wall parameters for each urban class (Table 1).

# b. Observations

The Automated Surface Observing System (ASOS) 10-m winds averaged at 2-min intervals (available every minute) are used from Palm Beach International Airport (KPBI), Miami International Airport (KMIA), and Pompano Beach Airpark (KPMP). Of these stations, only KPBI collected data during the entirety of Irma's outer-wind-field landfall on Miami. These are all airport stations, in more exposed locations. KMIA was close to, and downwind of, downtown Miami for much of the landfall. Stations at Fort Lauderdale/Hollywood International Airport (KFLL) and North Perry Airport (KHWO) are not used because they had insufficient data during landfall: KFLL stopped reporting at 2100 UTC 9 September and KHWO stopped reporting at 0400 UTC 10 September. One urban station is used: the University of Miami Health Center WeatherStem (WSUMH). The anemometer is on a Davis Instruments VantagePro2 weather station and is located on top of a building in downtown Miami at 65 m AGL. The WSUMH data are reported at a 1-min frequency. The standardization of these data to 10 m will be discussed in section 5e. The inflow winds to Miami are analyzed from the NOAA National Data

TABLE 1. Names and values of parameters in BEP for low-intensity residential (LIR), high-intensity residential (HIR), and commercial and industrial (COI) urban classes.

Parameter	LIR	HIR	COI
Roof/wall heat capacity (J m <sup>-3</sup> K <sup>-1</sup> )	$1.0 \times 10^{6}$	$1.0 \times 10^{6}$	$1.0 \times 10^{6}$
Ground heat capacity (J m <sup>-3</sup> K <sup>-1</sup> )	$1.4 \times 10^{6}$	$1.4 \times 10^{6}$	$1.4 \times 10^{6}$
Roof/wall thermal conductivity (J m <sup>-1</sup> s <sup>-1</sup> K <sup>-1</sup> )	0.67	0.67	0.67
Road thermal conductivity (J m <sup>-1</sup> s <sup>-1</sup> K <sup>-1</sup> )	0.4004	0.4004	0.4004
Roof/wall surface albedo	0.20	0.20	0.20
Road surface albedo	0.15	0.15	0.15
Roof/wall surface emissivity	0.90	0.90	0.90
Road surface emissivity	0.95	0.95	0.95
Roof/road/wall momentum roughness length (m)	0.01	0.01	0.01

Buoy Center Fowey Rocks station (FOW), which reports winds at a 10-min frequency. Finally, the observational wind swath analysis of Hagen et al. (2018) is used. It was produced from observed winds from numerous surface-based platforms and Weather Surveillance Radar-1988 Doppler (WSR-88D) velocity data. More details on the analysis procedures are provided in appendix B. One important point regarding the analysis is that the reduction factors are not based on local surface roughness. Thus it is possible that the analyzed winds in the urban environment might be biased high.

To evaluate the WRF simulations against the observations, the WRF diagnosed winds at 10 m AGL are used at a temporal frequency of 20 s. In comparing to the ASOS station data, the WRF winds are averaged using 2-min centered windows at the ASOS observation time. Hourly averages of the 20-s output from the WRF Model are used to compare to the hourly averages of the Fowey Rocks and WSUMH station data. No reduction factors are used to compare the WRF simulations to the ASOS data since they are both at 10 m AGL. The reduction factors applied to the Fowey Rocks and WSUMH elevated data are described in sections 5c and 5e, respectively.

Important issues in comparing model simulations to observations are observational sampling biases and what our simulations can resolve at their effective resolutions. The spatial sparseness of the observations described above does not permit adequate sampling of small-scale structures in the PBL. Similarly, our model simulations cannot well resolve features in the HBL with horizontal scales less than 3–4 km. Although these sampling and representativeness issues are partially mitigated when we evaluate temporally and spatially averaged quantities, there is more uncertainty in our time series and TKE analysis.

### c. Land-use, urban fraction, and building heights

In Fig. 2, the locations of KPBI, KPMP, KMIA, WSUMH, and FOW are shown on three different panels. In Fig. 2a, the stations are plotted on the 33-category Modified International Geosphere–Biosphere Programme (IGBP) Moderate Resolution Imaging Spectroradiometer (MODIS) Noah land-use categories (Table 2). The land-use categories of 31, 32, and 33 correspond to low-intensity residential (LIR), high-intensity

residential (HIR), and commercial and industrial (COI). The Miami metropolitan area has two distinct urban clusters, downtown Miami and Fort Lauderdale, denoted by the areas of land-use categories 32 and 33. Higher urban fractions are evident in downtown Miami, Fort Lauderdale, and Palm Beach (Fig. 2b). According to the 1-km gridded average value from NUDAPT, the tallest buildings are in downtown Miami, with peak values of building height weighted by plan area of around 30-35 m (Figs. 2c,d). Another maximum exists north in Fort Lauderdale, with peak values around 10-15 m. Miami International Airport (KMIA) is near a built-up area, and the Miami Health Center WeatherStem station is near some of Miami's tallest buildings (Fig. 2d). The parameter in Figs. 2c and 2d is not the actual building height, but the height weighted by plan area, and the NUDAPT gridding at 1-km inherently will reduce the heights from reality. Hereafter, "downtown Miami" will refer to the area near KMIA and WSUMH, and the "Miami metropolitan area" will refer to the entire north-south-oriented urban area (land-use category of 31 or greater) from south of downtown Miami to north of West Palm Beach (KPBI).

### 5. Results

### a. Track and intensity forecasts

In Fig. 3, the simulated track and intensity forecasts are compared to the NHC best track. The storm center is defined by the minimum surface pressure on domain 3 ( $\Delta x = 2 \text{ km}$ ) (no smoothing is applied prior to center finding). The maximum horizontal velocity at  $z = 10 \,\mathrm{m}$  AGL within 150 km of the storm center is used as a proxy for the peak near-surface winds in the eyewall at a given time. Simulated positions and intensity estimates are obtained at the model output times on domain 3 every 10 min. To compare to the 6-hourly NHC best track data, the simulated values are averaged over centered ±3-h windows using 36 different model output times. Although we are not able to compute a 1-min maximum sustained wind on domain 3 due to the 10-min output, Uhlhorn and Nolan (2012) have shown that the instantaneous 10-min wind typically only underestimates the 1-min maximum sustained wind by 1.5% because of the sufficiently large spatial scale of the wind anomalies in hurricanes.

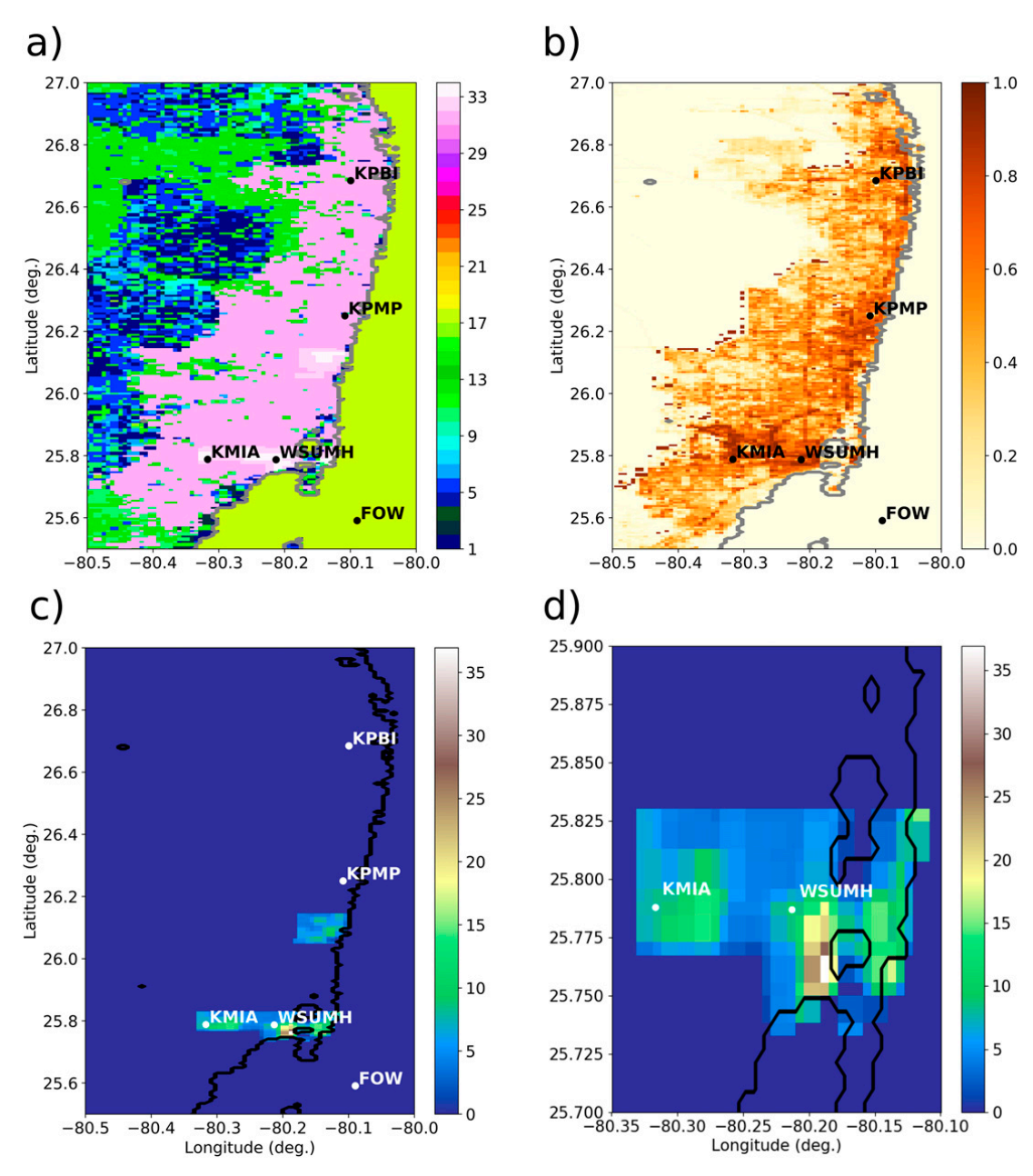


FIG. 2. Urban characteristics of the Miami metropolitan area on domain 4 ( $\Delta x = 0.67$  km). (a) USGS 33-category land-use index, (b) urban fraction, (c) average building height weighted by building plan area, and (d) zoomed-in average building heights weighted by plan area in downtown Miami. The locations of the stations KMIA, KPMP, KPBI, WSUMH and FOW are plotted in (a)–(c), and the locations of KMIA and WSUMH are plotted in (d).

The tracks of the simulated storms match the NHC best track quite well (Fig. 3a) in terms of both along- and cross-track errors. The average track errors from 1200 UTC 9 September to 0000 UTC 11 September are 37.4, 37.1, 33.9, and 32.5 km, in the MYJ BULK, MYJ BEP, YSU BULK, and YSU BEP simulations, respectively. Overall, the YSU BULK simulation matches the NHC best track positions the best during the period of highest winds in Miami from 0600 to 1800 UTC 10 September.

The MYJ BEP, YSU BULK, and YSU BEP simulations have negative intensity biases around 5 m s<sup>-1</sup> before 1800 UTC

10 September and have positive biases of similar magnitude after that time (Fig. 3b). The MYJ BULK simulation has a larger negative bias of approximately 10 m s<sup>-1</sup> before 1800 UTC 10 September. The average intensity errors from 1200 UTC 9 September to 0000 UTC 11 September are 6.5, 3.9, 4.2, and 4.7 m s<sup>-1</sup>, in the MYJ BULK, MYJ BEP, YSU BULK, and YSU BEP simulations, respectively. While the positive intensity biases after 1800 UTC 10 September are explainable because the simulated storms tracked closer to the warm Gulf of Mexico waters, exposing more of the circulation to higher

TABLE 2. Modified IGBP MODIS Noah land-use indices and descriptions.

F				
Land-use index	Description			
1	Evergreen needleleaf forest			
2	Evergreen broadleaf forest			
3	Deciduous needleleaf forest			
4	Deciduous broadleaf forest			
5	Mixed forests			
6	Closed shrublands			
7	Open shrublands			
8	Woody savannas			
9	Savannas			
10	Grasslands			
11	Permanent wetlands			
12	Croplands			
13	Urban and built-up			
14	Cropland/natural vegetation mosaic			
15	Snow and ice			
16	Barren or sparsely vegetated			
17	Water			
18	Wooded tundra			
19	Mixed tundra			
20	Barren tundra			
31	Low-intensity residential			
32	High-intensity residential			
33	Industrial or commercial			

moist entropy fluxes, the reasons for the negative intensity biases beforehand are not as obvious. Possibilities include not using a vortex bogussing technique or not capturing the complexity of the air-ocean interaction over the Florida Strait, Keys, and Florida Bay. The simulations do capture the intensification trend over the Florida Straits and weakening after hitting Cudjoe Key and moving into the Florida Bay. Considering

the challenges of simulating Irma, such as the abrupt recurvature, interaction with Cuba and Florida, and the complex ocean conditions (deep mixed layer over the Florida Straits and shallower waters in the Keys and Florida Bay), the intensity forecasts are of sufficient accuracy for this study. Our primary focus is obtaining a realistic forecast of the outer wind field structure and inflow winds to Miami, and not necessarily a perfect forecast of the overall storm track and intensity. We will examine the veracity of the simulated outer wind fields in sections 5b and 5c.

### b. Wind field structure at 10 m AGL

To assess the surface wind structure, the simulations are evaluated against the National Oceanic and Atmospheric Administration (NOAA) Regional and Mesoscale Meteorology Branch (RAMMB) aircraft-based tropical cyclone surface wind analysis (TCSWA). This is a real-time product that blends a multiplatform satellite wind analysis with aircraft reconnaissance data (Knaff et al. 2015; Zhang and Uhlhorn 2012). The inner core is mostly determined by the aircraft reconnaissance data, while the outer field uses both the aircraft and satellite data.

We first compare the wind fields at 1200 UTC 10 September (Fig. 4a), when Irma made its first U.S. landfall on the Florida Keys. All simulations compare favorably at this time in terms of the locations of the eye and eyewall. The TCSWA inner core is more compact than in the WRF Model simulations, and the peak winds are slightly weaker. The TCSWA has winds at  $35 \,\mathrm{m\,s^{-1}}$  at the southern end of Key Biscayne,  $25 \,\mathrm{m\,s^{-1}}$  in downtown Miami, and  $20 \,\mathrm{m\,s^{-1}}$  north of Miami. All WRF Model simulations have similar wind speeds to the TCSWA over the ocean near Miami, and slightly stronger winds than the TCSWA farther north along the coast toward West Palm Beach. One of most striking differences between the WRF

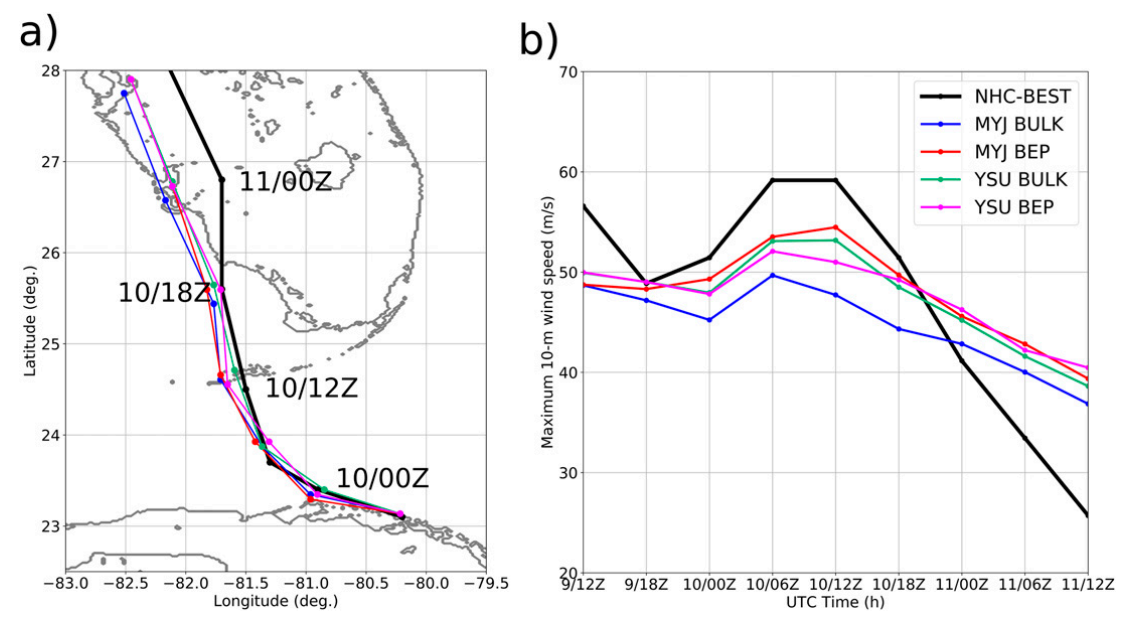


FIG. 3. (a) Observed and simulated tracks and (b) intensities. The NHC best track is in black, and the four simulations are in different colors. In each panel, markers are every 6 h.

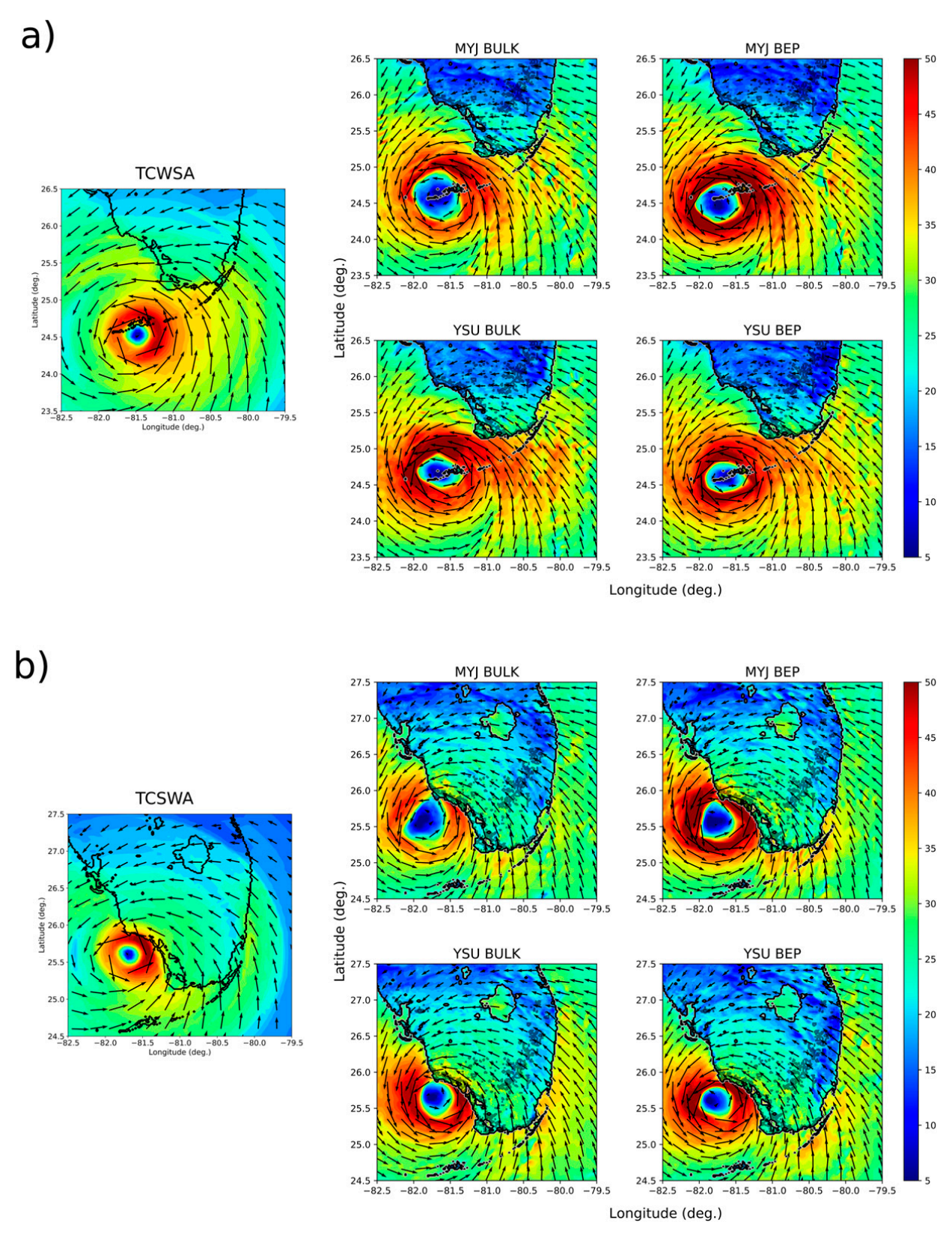


FIG. 4. (left) NOAA RAMMB 10-m tropical cyclone surface wind analysis (TCSWA) using aircraft data, and the four WRF Model simulations' 10-m winds valid at (a) 1200 UTC 10 Sep 2017 and (b) 1800 UTC 10 Sep 2017. Wind speeds are in m s<sup>-1</sup>, and vectors are overlaid. The TCSWA wind vectors are plotted every five analysis grid points, and the simulation vectors are plotted every seven model grid points. The vector tail is at the analysis or model grid point, and the head is downwind.

Model simulations and the TCSWA is the distribution of wind speeds over land. All WRF Model simulations have much weaker near-surface winds over the urban and rural areas than does the TCSWA. The TCSWA has a relatively simplistic overland wind adjustment: a 20% reduction in wind speed and 20° turn to the left owing to surface friction (Knaff et al. 2015). BEP is active on domains 3 and 4, and the urban wind speed is lower in the MYJ and YSU BEP simulations at this time.

At the time of Irma's second landfall near Marco Island, Florida (Fig. 4b; 1800 UTC 10 September), all WRF Model simulations match the TCSWA position quite well. There is some variability in the intensity of the different simulations at landfall. The TCSWA has a weaker north-south-oriented area of winds in the urban sector (around  $20\,\mathrm{m\,s^{-1}}$ ). The simulations capture the stronger TCSWA ocean winds just east of Miami reasonably well. The MYJ and YSU BEP simulations have slight reductions in urban winds in comparison to their BULK counterparts at this time. At both times, the simulated storms have more expansive wind fields than the TCSWA over the Atlantic Ocean, just east of the Florida peninsula.

A quantitative analysis of Irma's size (outer wind field structure and magnitude) at 1200 and 1800 UTC 10 September is given in Figs. 5a and 5b, respectively. The Cartesian horizontal velocity components are first converted to radial and tangential velocity components about the center of Irma in the simulations and in the TCSWA. Then, the WRF simulation and TCSWA data at 10 m AGL are interpolated to a polar grid with a radial grid spacing of 2 km and azimuthal spacing of 0.125 66 radians. Finally, at each radius, the radial, tangential, and total velocities are azimuthally averaged. At 1200 UTC 10 September (Fig. 5a), beyond  $r = 150 \,\mathrm{km}$ , the WRF simulations have slightly higher velocities than the TCSWA and slightly lower velocities than the NHC best track winds at the outer wind radii (radii of 34- and 50-kt winds; 17.5 and 25.7 m s<sup>-1</sup>, respectively). At Miami, the azimuthal mean tangential and radial velocities are similar among the WRF simulations and the TCSWA, while more significant differences exist near Irma's core. At 1800 UTC 10 September (Fig. 5b), similarly, the WRF simulations have slightly higher outer velocities than the TCSWA overall, and slightly lower velocities than the NHC best track winds at the outer radii. The azimuthal mean tangential and radial velocities are also similar among all WRF simulations and the TCSWA at the location of Miami. This analysis indicates that the simulated outer wind field structure of Irma is sufficiently accurate to examine the urban winds in Miami.

### c. Time series of inflow winds to downtown Miami

The inflow winds to Miami are analyzed from the NOAA National Data Buoy Center Fowey Rocks station. The anemometer height is 43.9 m above sea level. A factor of 0.95 is used to reduce these winds to an equivalent 10-m inflow wind for comparison with the WRF Model simulations. While there is some uncertainty as to what these reduction factors should be for individual cases, our choice is based on the hurricane outer wind field dropwindsonde composite [as

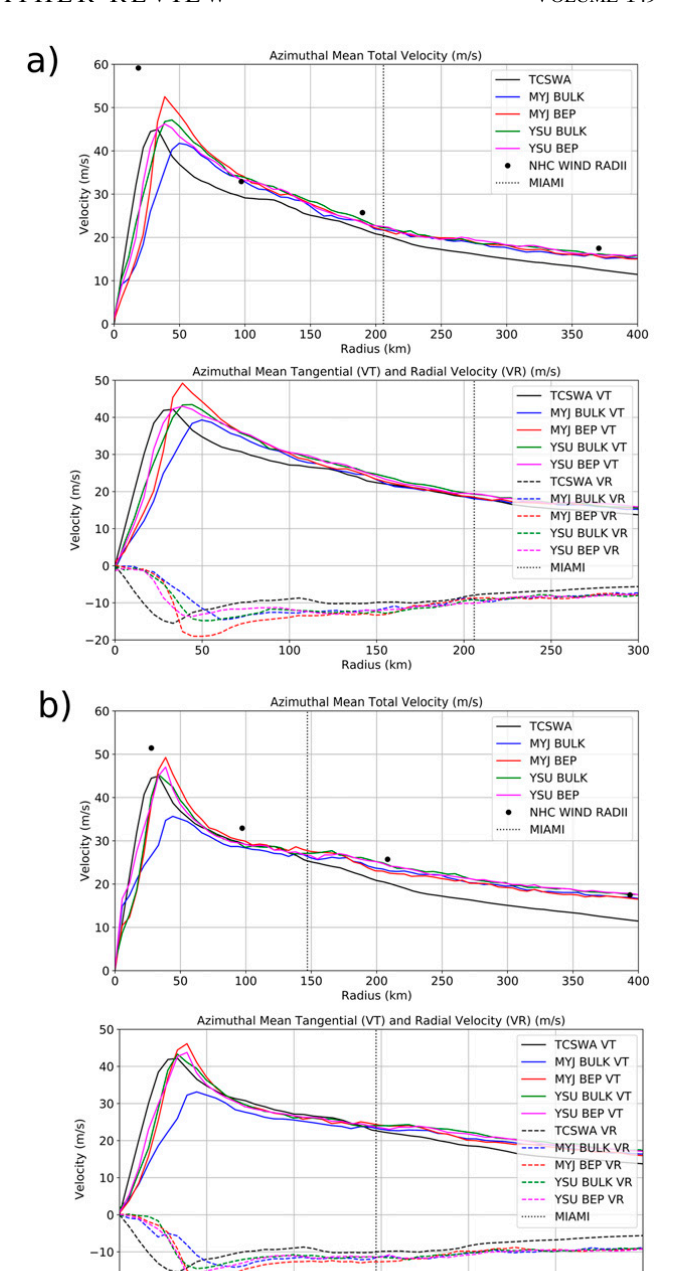
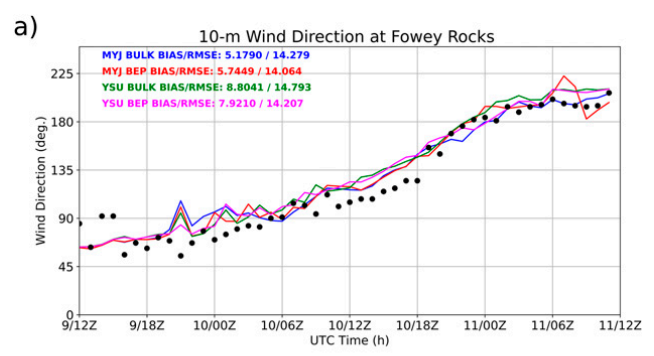


FIG. 5. Azimuthal mean wind structure at 10 m AGL of the total velocity, and tangential and radial components in the TCSWA and the WRF simulations: (a) 1200 UTC 10 Sep 2017 and (b) 1800 UTC 10 Sep 2017. In the total velocity panels, the NHC best track wind radii and corresponding velocity are shown in solid black circles: the radii of the radius of maximum winds and maximum 1-min sustained wind, radius of 64-kt (32.9 m s<sup>-1</sup>) winds, radius of 50-kt winds (25.7 m s<sup>-1</sup>), and radius of 34-kt (17.5 m s<sup>-1</sup>) winds. NHC wind radii are averaged over all four quadrants. The location of Miami in relation to the storm center is marked by the dotted vertical line. The TCSWA and WRF simulation wind profiles include the storm motion vector.

150 Radius (km)

100

shown in Fig. 8 of Franklin et al. (2003)]. No adjustment is made for wind direction. Based upon dropwindsonde data [Fig. 6 of Smith and Montgomery (2014a)], wind direction changes from 0 to 50 m are very small over water. Simulated



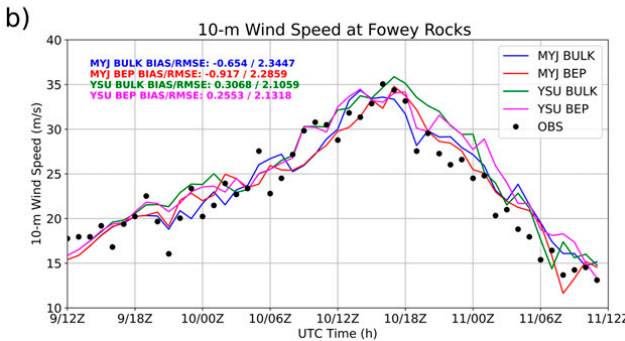


FIG. 6. Inflow 10-m wind vector to Miami at Fowey Rocks from observations and WRF Model domain 4: (a) wind direction (°) and (b) wind speed (m s<sup>-1</sup>). The hourly observations are denoted by black dots and the simulations are in different colors. The number of observation and simulation points used to compute biases and RMSEs is N = 48.

time series from domain 4 are extracted at the nearest model grid point to Fowey Rocks (25.591°N, 80.097°W). The observational data are given as hourly averages, and thus the 20-s output on domain 4 is averaged each hour for the comparison. Although we could compare the model output interpolated to a height 43.9 m, since our focus is on near surface inflow winds and the 20-s near-surface output from domain 4, it is more appropriate to reduce the observations to an equivalent 10-m value. For this and other evaluations in this paper we use the traditional statistical performance measures of the mean error,  $ME = \overline{M} - \overline{O}$ , (or bias) and root-mean-squared error,  $RMSE = \left[\sum_{i=0}^{N} (M_i - O_i)^2/N\right]^{1/2}$ , wherein M is the model simulation value at the observation location, and O is the observational value. Overbars denote the mean value of all model simulations or observations. The number of evaluation points is N.

All simulations compare reasonably well to the observed time series (Fig. 6). Wind directions are biased from  $+5^{\circ}$  to  $+8^{\circ}$ , indicating that the simulated winds into Miami are slightly too southerly with too small an inflow angle. Nolan et al. (2021b) also found that their Hurricane Wilma (2005) simulations had too small an inflow angle in comparison to observations. Wind direction RMSEs are  $14^{\circ}$  on average. Wind speed biases are low, ranging from approximately -0.9 to  $0.3\,\mathrm{m\,s^{-1}}$ . Wind speed RMSEs are also low, around  $2.2\,\mathrm{m\,s^{-1}}$ . In summary, all simulations capture the observed change of the wind direction from easterly to southerly over the  $48\,\mathrm{h}$  and the timing and magnitude of peak onshore winds to Miami. After the peak winds at  $1800\,\mathrm{UTC}\,10$  September, all

simulations have wind speeds that are slightly stronger than the observations.

# d. Areal analysis of simulated winds and BEP momentum sinks in the Miami metropolitan area

A detailed plan view of the 10-m winds near the time of peak inflow winds (1800 UTC 10 September) is given in Fig. 7a. First, comparing the simulations with the BULK scheme, the MYJ simulation has slightly weaker winds than the YSU simulation in downtown Miami, near the coast, and in the urban area west of the coast. The same is true over the ocean. The MYJ and YSU BEP simulations have weaker winds in the urban area than their BULK simulation counterparts (particularly north of downtown Miami and just west of the coast). Overall, the BEP wind speed reductions over BULK in the YSU simulations are greater than they are in the MYJ simulations (Fig. 7b). An interesting aspect of these plots is the magnitude of the BEP simulations' reduction of the wind in the city. Winds over the ocean are 30-35 m s<sup>-1</sup> and decrease to 10-20 m s<sup>-1</sup> moving west into the urban area. All simulations have stronger winds of 25–30 m s<sup>-1</sup> at coastal locations (e.g., Miami Beach), for which there is also observational support (discussed further in section 5f). The rapid reduction in nearsurface winds as a result of enhanced surface roughness is consistent with the study by Hirth et al. (2012).

To understand why the BEP simulations have lower urban winds than the BULK simulations, it is instructive to recall that BEP has implicit A and explicit B momentum sources. These components contain both the effects of drag from horizontal (roofs and roads) and vertical (building walls) surfaces, as well as from the rural horizontal sources. The rural sources are in the implicit component A, while all urban sources are in the explicit component B, except one-half of the vertical surface source. To illustrate the urban forcing near the time of peak winds, in Fig. 8a, the magnitude of the explicit component B for momentum is given for the MYJ BEP and YSU BEP simulations at 1800 UTC 10 September, with B vectors overlaid. As strong winds impinge on Miami, the B momentum sink due to the drag force decelerates this inflow, reducing the urban winds in the Miami metropolitan area. Both simulations have large momentum sinks right near the coast, where near hurricaneforce winds first impinge on the built-up area. The YSU BEP simulation has smaller B momentum sinks in the Miami metropolitan area than the MYJ BEP simulation away from the coast, and larger sinks along the coast (Fig. 8b). The total source S = AC + B exhibits similar structures, but with larger magnitudes because rural sources are included in the implicit A components.

### e. Areal analysis and time series of TKE

The eddy viscosity K is proportional to the TKE in the MYJ PBL parameterization (section 3). TKE in the Miami metropolitan area is  $15-20\,\mathrm{m^2\,s^{-2}}$  in the MYJ BULK simulation and  $5-10\,\mathrm{m^2\,s^{-2}}$  in the MYJ BEP simulation (Fig. 9). Larger values exist on the coast in both simulations. While TKE is produced by buildings (an extra source term in BEP), the turbulence length scale is reduced (2) leading to enhanced dissipation of TKE in the budget equation. The MYJ BEP simulation has

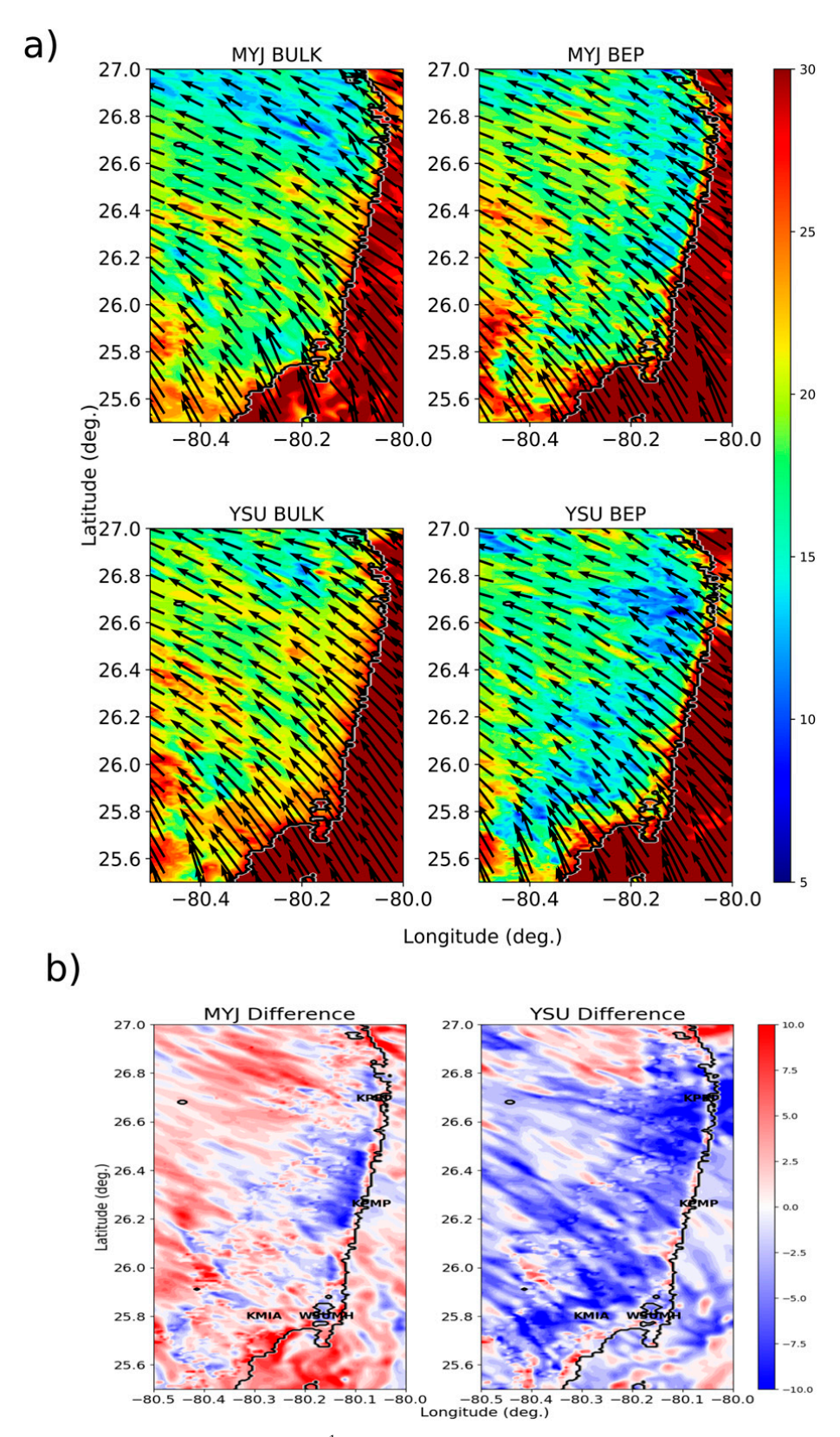


FIG. 7. (a) 10-m wind speed (m s $^{-1}$ ) and overlaid vectors (every 12 model grid points) in the Miami metropolitan area at 1800 UTC 10 Sep 2017 from all four WRF simulations and (b) the BULK simulations minus the BEP simulations.

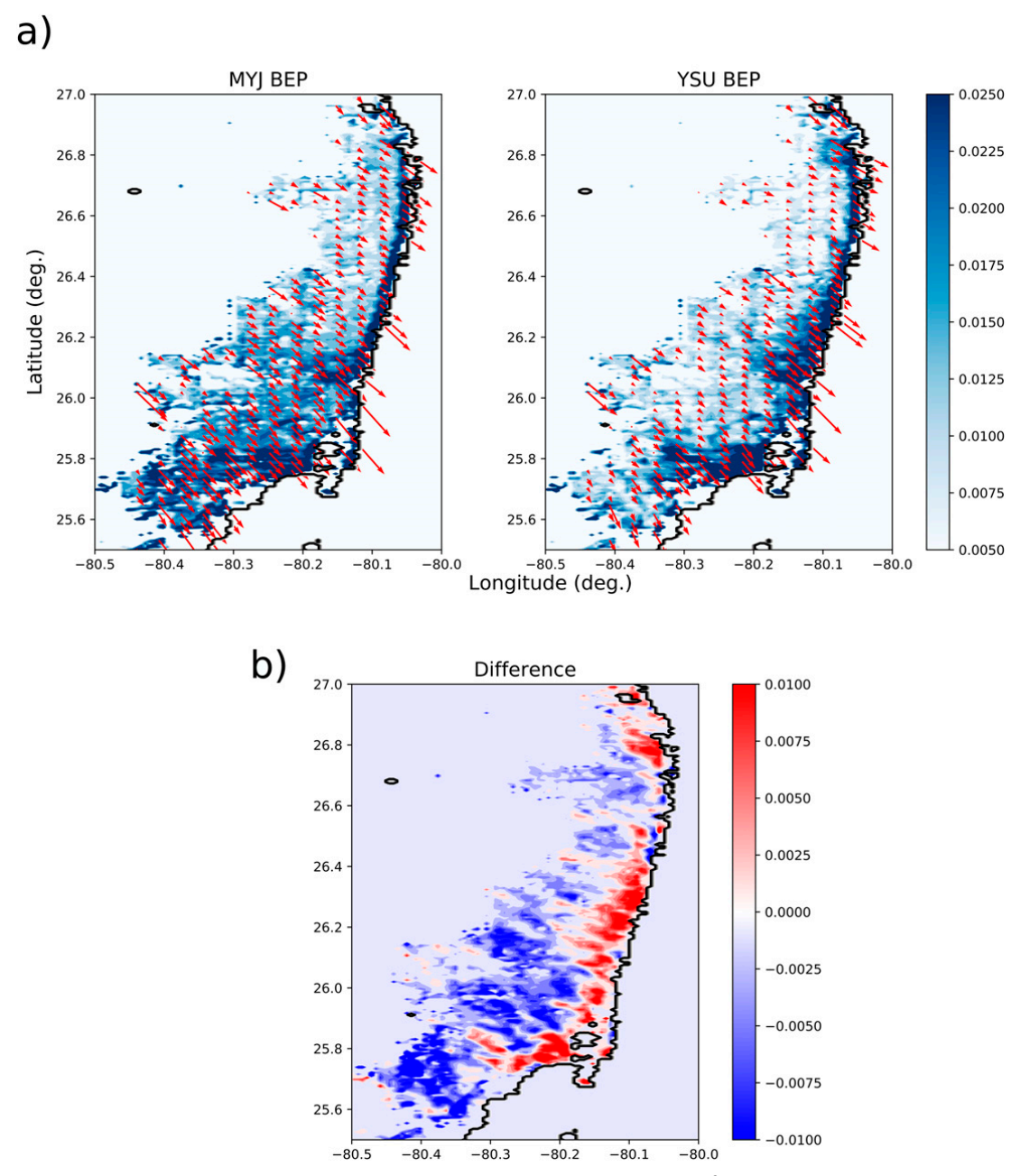


FIG. 8. (a) Explicit component B for the horizontal momentum tendency (m s<sup>-2</sup>) on WRF Model domain 4 in the Miami metropolitan area in the (left) MYJ BEP and (right) YSU BEP simulations at 1800 UTC 10 Sep, with B vectors overlaid at intervals of five grid points, and (b) difference field: YSU BEP minus MYJ BEP. The contour levels span a slightly smaller range than the data in order to better illustrate the smaller values of the data.

lower TKE in Miami than the MYJ BULK simulation, presumably because the TKE dissipation term is dominant over the building TKE source term. The lower TKE in the MYJ BEP simulation reduces the eddy viscosity coefficient there, causing reduced low-level local vertical mixing.

To understand the accuracy of the simulated TKE, we can estimate the observed TKE from the ASOS stations of KPBI, KMIA, and KPMP. The ASOS stations report two-dimensional winds (zonal and meridional components) at a lower frequency of 1 min, and thus are not suitable for an accurate direct TKE calculation; three-dimensional wind

measurements at a higher frequency (e.g.,10–20 Hz) would be needed. However, we estimated TKE from the ASOS stations using two different approaches based on gust factors: a direct method and an empirical method. These methods are described in appendix C. In each method, there is some uncertainty in the TKE due to inadequate temporal sampling.

Figure 10 shows the time series of the TKE estimates in comparison to the MYJ BULK and MYJ BEP simulated TKE at the first model level of 26.5 m at 10-min output frequency. Each observational time series shows data at 1-min frequency and also a smoothed curve. Smoothing is accomplished using a

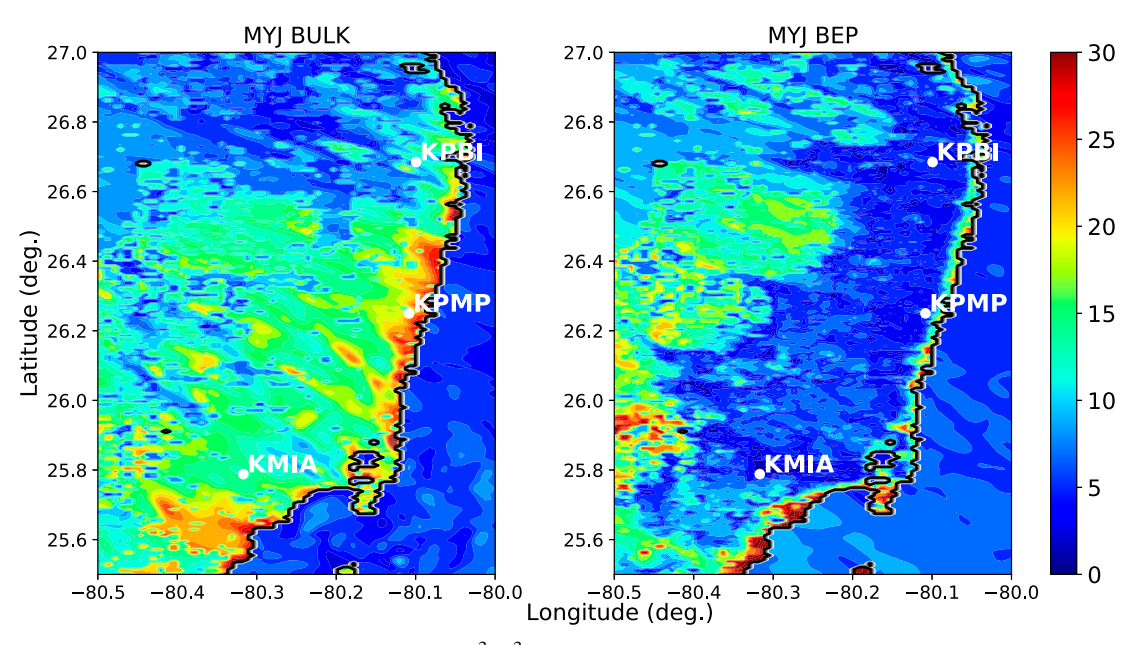


FIG. 9. (left) MYJ BULK simulation TKE ( $m^2 s^{-2}$ ) on domain 4 at z = 26.5 m and 1800 UTC 10 Sep, and (right) MYJ BEP simulation TKE on domain 4 at z = 26.5 m and 1800 UTC 10 Sep. The locations of the stations KMIA, KPMP, and KPBI are plotted in each panel.

low-pass Savitsky-Golay filter with a centered window of 51 points and cubic polynomials. The observed TKE from KPBI has a peak near the time of peak winds (1800 UTC 10 September). The KMIA and KPMP data end before this time; however, similar trends exist as at KPBI. At KMIA and KPMP (Figs. 10a,b), the MYJ BULK simulation predicts higher TKE than the observational estimates, while the MYJ BEP simulation is more consistent with the observational estimates. The time series of the observations ends before the peak winds, therefore we cannot state which simulation is more accurate at the time of peak winds. At KPBI (Fig. 10c), the MYJ BEP and MYJ BULK simulations are more similar to each other. The MYJ BULK simulation has a positive bias of  $2.5-5.0 \text{ m}^2 \text{ s}^{-2}$  at the time of peak winds (1800 UTC 9 September). KMIA and KPMP are closer to areas with larger buildings (downtown Miami and Fort Lauderdale, respectively, Fig. 2c). This proximity may partially explain why the MYJ BEP and MYJ BULK TKE values are significantly different there, where BEP buildinginduced TKE effects are larger. The observational estimates are slightly lower than open-ocean TKE calculated from Doppler radar observations in the HBL by Lorsolo et al. (2010)  $(4-6 \text{ m}^2 \text{ s}^{-2} \text{ in the outer wind field at } 1.5-2.0 \text{ times the}$ radius of maximum wind; their Fig. 7). Our TKE estimates are also broadly consistent with in situ aircraft observations in the outer rainbands of tropical cyclones (Zhang et al. 2009; Ming et al. 2014).

# f. Evaluation of simulations at fixed locations in the urban environment

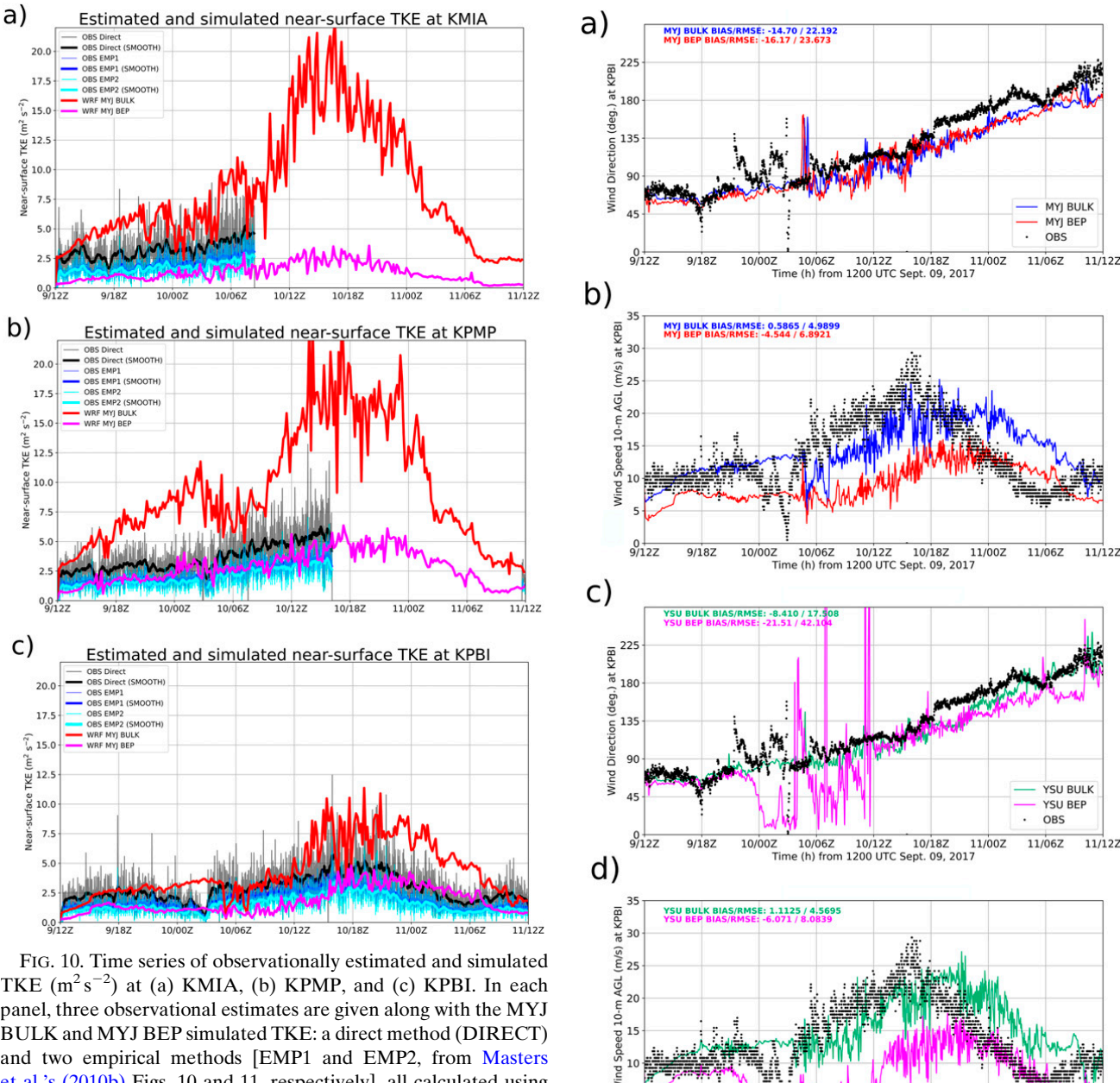
We now evaluate the simulations against surface stations in the Miami metropolitan area. Time series analysis is conducted at the following stations: KPBI, KMIA, KPMP, and WSUMH. The WRF Model domain 4 winds must be converted

to open-exposure values for comparison to airport stations (KPBI, KMIA, KPMP). The urban WeatherStem station WSUMH is not in an exposed location, therefore the WRF Model winds are not converted to open exposure there. The open exposure conversion is done according to Nolan et al. (2021a):

$$\mathbf{u}_{10\text{m,open}}(x,y) = \mathbf{u}_{10\text{m}}(x,y) \frac{\ln[z_{\text{ref}}/z_0(x,y)]}{\ln[10/z_0(x,y)]} \frac{\ln(10/z_{\text{open}})}{\ln(z_{\text{ref}}/z_{\text{open}})}, \quad (6)$$

wherein,  $\mathbf{u}_{10\text{m},\text{open}}(x,y)$  is the open-exposure-corrected velocity vector,  $\mathbf{u}_{10\text{m}}(x,y)$  is the original vector from domain 4 of the WRF Model simulations,  $z_{\text{ref}} = 50\,\text{m}$  is a reference height,  $z_0(x,y)$  is the surface roughness, and  $z_{\text{open}} = 0.03\,\text{m}$  is an open exposure roughness length. Because the 10-m winds in the WRF Model are diagnosed values using the roughness, low-level stability, and other factors, one can take a similar approach to diagnose an equivalent open-exposure wind using a lower roughness value indicative of openly exposed areas (Nolan et al. 2021a). Finally, as discussed in section 4b, the WRF Model 20-s output on domain 4 is averaged to 2 min (centered windows) to compare to the ASOS 2-min averages.

At KPBI, the wind direction is reasonably well predicted by both the MYJ BULK and BEP simulations, although the winds are a little more easterly than the observations by approximately 14°–16° (Fig. 11a). Both simulations lag the observations by approximately 3 h in the timing of peak winds (Fig. 11b). The MYJ BULK simulation has a small positive bias of 0.59 m s<sup>-1</sup> while the MYJ BEP simulation has a negative bias of -4.5 m s<sup>-1</sup>. The YSU BULK and BEP simulations also have easterly wind direction biases of 8.4° and 21.5°, respectively. The YSU simulations also have a lag in the timing of peak winds of approximately 5 h. The YSU BULK simulation has a small positive wind bias of 1.1 m s<sup>-1</sup>, while the YSU BEP



TKE (m<sup>2</sup> s<sup>-2</sup>) at (a) KMIA, (b) KPMP, and (c) KPBI. In each panel, three observational estimates are given along with the MYJ BULK and MYJ BEP simulated TKE: a direct method (DIRECT) and two empirical methods [EMP1 and EMP2, from Masters et al.'s (2010b) Figs. 10 and 11, respectively], all calculated using gust factors. The observational estimates are plotted at 1-min frequency along with smoothed curves (SMOOTH) constructed with the Savitzsky-Golay digital filter. The WRF Model simulations are plotted at 10-min output frequency and at a height of  $z = 26.5 \,\mathrm{m}$ .

simulation has a larger negative bias of  $-6.1 \,\mathrm{m\,s}^{-1}$ . Overall, the BULK simulations are superior to the BEP simulations at KPBI, but even the BULK simulations have peak winds that are approximately 5 m s<sup>-1</sup> too low. There is rapid variability in the wind speed and direction in the observations between 0000 and 0600 UTC 10 September, which is not well captured by the WRF simulations. The YSU BEP simulation winds are significantly too weak in comparison to the observations between 0000 and 1200 UTC 10 September, and the wind direction becomes more variable (note that apparent largest variations are due to the winds turning from above to below  $0^{\circ}$ ).

FIG. 11. Time series of 2-min average observations and WRF Model domain 4 model simulations at Palm Beach International Airport (KPBI): (a) MYJ BULK and BEP wind direction, (b) MYJ BULK and BEP wind speed (m s<sup>-1</sup>), (c) YSU BULK and BEP wind direction, and (d) YSU BULK and BEP wind speed (m s<sup>-1</sup>). Observations and model-simulated values are at 10 m AGL. The number of observation and simulation points used to compute biases and RMSEs is N = 2880.

9/18Z

10/06Z 10/12Z 10/18Z 1 (h) from 1200 UTC Sept. 09, 2017

11/00Z

The KMIA observations end around 0800 UTC 10 September, before the time of peak winds, and therefore the simulations can only be compared up until this time. Similar to KPBI, wind directions are generally predicted well but with a slight easterly bias of 2°-7° (Figs. 12a,c). The BULK simulations also have

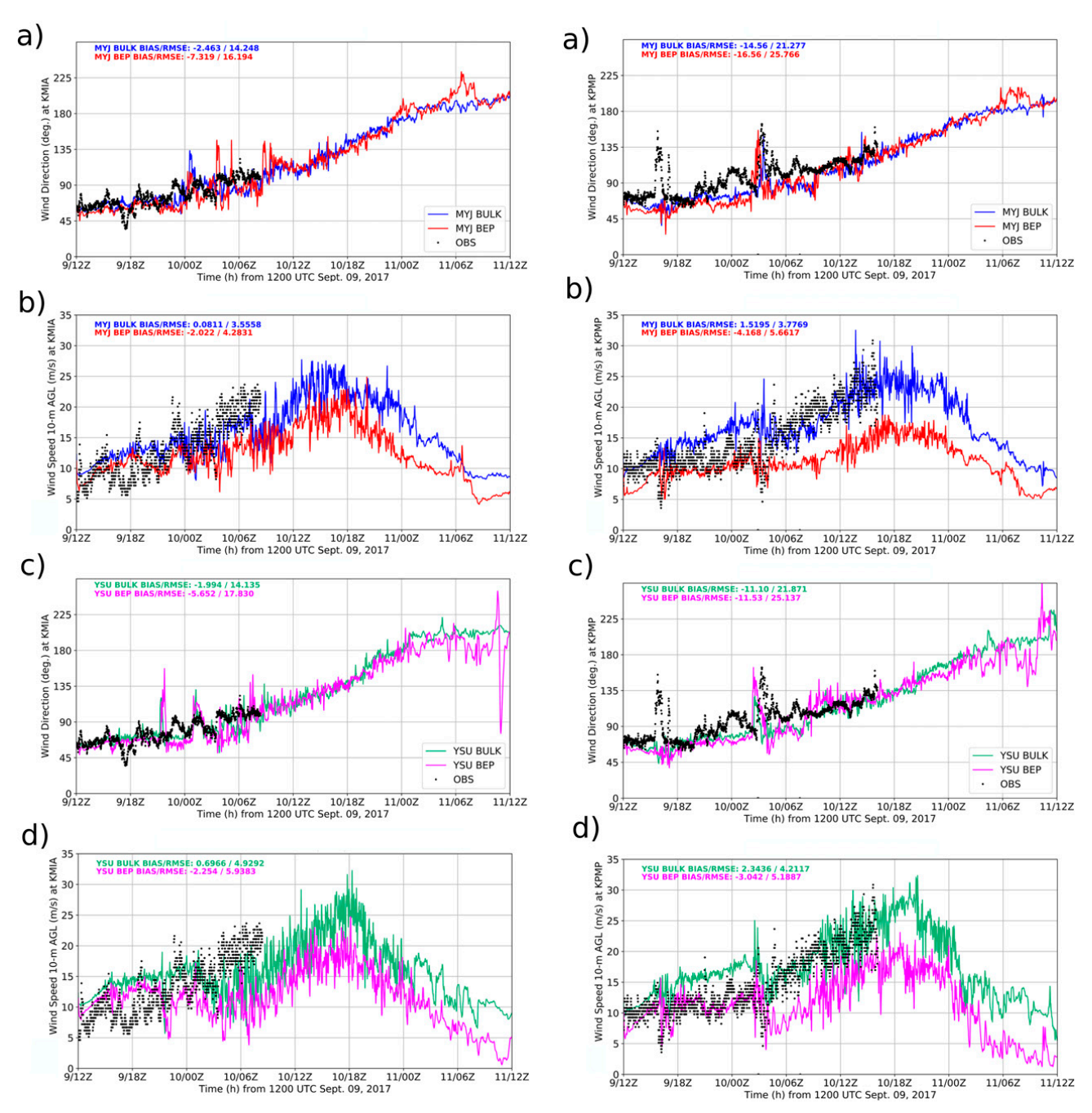
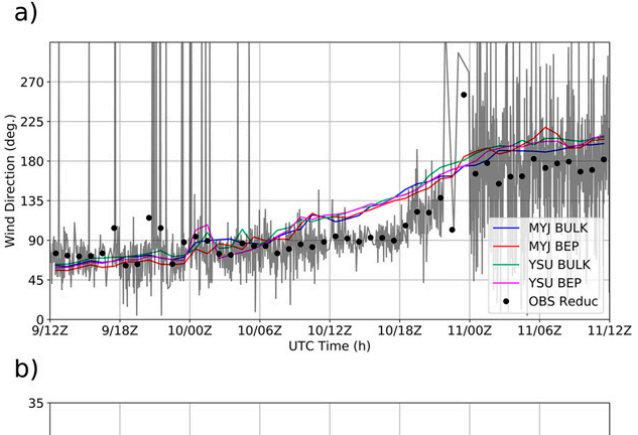


FIG. 12. Time series of 2-min average observations and simulations on domain 4 of the WRF Model at Miami International Airport (KMIA): (a) MYJ BULK and BEP wind direction, (b) MYJ BULK and BEP wind speed (m s<sup>-1</sup>), (c) YSU BULK and BEP wind direction, and (d) YSU BULK and BEP wind speed (m s<sup>-1</sup>). Observations and model simulated values are at 10 m AGL. The number of observation and simulation points used to compute biases and RMSEs is N = 1223.

FIG. 13. Time series of 2-min average observations and simulations on domain 4 of the WRF Model at Pompano Beach Airpark (KPMP): (a) MYJ BULK and BEP wind direction, (b) MYJ BULK and BEP wind speed (m s<sup>-1</sup>), (c) YSU BULK and BEP wind direction, and (d) YSU BULK and BEP wind speed (m s<sup>-1</sup>). Observations and model simulated values are at  $10 \,\mathrm{m}$  AGL. The number of observation and simulation points used to compute biases and RMSEs is N = 1688.

more accurate wind speeds than the BEP simulations. The BEP negative biases in wind speed at KMIA are smaller than at KPBI. MYJ BEP and YSU BEP biases are approximately 2 m s<sup>-1</sup> (Figs. 12b,d). The KPMP observations end near 1600 UTC 10 September, which is near the time of peak winds

in Miami. Similar to KPBI and KMIA, wind directions are predicted well at KPMP (Figs. 13a,c). The BULK simulation wind speed predictions at KPMP are very good leading up to the time of peak winds (0600–1800 UTC 10 September) and better overall than corresponding BEP simulations. The BEP



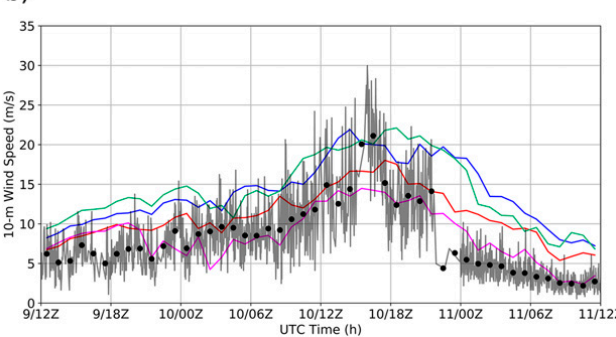


FIG. 14. Hourly averaged observations and WRF Model domain 4 simulations of (a) wind direction and (b) wind speed (m s<sup>-1</sup>) at WSUMH. Observations at 65 m are reduced to 10 m using a 0.615 reduction factor based on a log profile with an aerodynamic roughness length of 0.5 m for an urban environment (Reduc). The 1-min frequency observational data are shown in transparent black in both panels.

simulations have negative biases of  $3-4\,\mathrm{m\,s^{-1}}$  while the BULK simulations have positive biases of  $1-2\,\mathrm{m\,s^{-1}}$  (Figs. 13b,d). No simulations are able to capture the rapid southerly turning of the wind direction at 1600 UTC 9 September, maybe because this time is within the model spinup period, only 4 h after initialization.

In Fig. 14, we compare the simulations to the observations at WSUMH, which is in a less exposed urban location (Fig. 2). The WSUMH observations at 65 m are reduced to 10 m by applying a reduction factor  $r = \ln(10.0/z_{0u})/\ln(65.0/z_{0u}) =$ 0.615, obtained from a log profile assumption with an aerodynamic urban roughness length of  $z_{0u} = 0.5 \,\mathrm{m}$ . The 0.615 reduction factor is also consistent with the average reduction factor in the WRF simulations from 65 to 10 m AGL over the urban environment. At WSUMH, the simulated wind directions agree reasonably well with the observations with a gradual turning from easterly to southerly. However, the simulations transition to southerly earlier and more gradually than the observations. It is interesting to note the sharp drop off in wind speed in the observations after the time of peak winds. This happens coincident with the turning of the winds to southerly (Fig. 14a), therefore it is possible that buildings in the vicinity of this station are sheltering the station more under specific wind directions. The BEP simulations match the observations best prior to 2100 UTC 10 September. All simulations have winds that are too strong in comparison to the reduced observations; however, the BEP simulations perform better than the BULK simulations for each PBL scheme. Without a dense network of near-surface sheltered urban stations, it is not possible to make any general conclusion on whether the BULK or BEP simulations produce more realistic winds in the built-up area of downtown Miami. However, the BEP simulations perform best at these two urban stations.

#### g. Analyzed and simulated wind swaths

The observational analysis (Hagen et al. 2018) and simulated 1-min sustained wind swaths at 10 m AGL are presented in Fig. 15. The simulated wind swaths are computed by performing centered-in-time 1-min averages on the 20-s WRF Model domain 4 winds, and then taking the maximum value of this quantity over the entirety of the 48-h simulation time period at each model grid point. The simulated winds are converted to open exposure for this comparison as well (6). The analyzed wind swath depicts a west-east gradient of peak winds across southern Florida. In the Miami metropolitan area and just west, the winds are weakest with speeds of approximately 25 m s<sup>-1</sup>. Wind speeds are dramatically higher near Naples with peak values near 40 m s<sup>-1</sup>. The simulated wind swaths also depict this west-east gradient reasonably well; however, there are many differences among the different simulations. First, the analyzed wind swath does not contain observations over the ocean, so we cannot assess which WRF Model simulations perform best there. Second, the WRF Model simulations reveal streaks of high wind speeds that are approximately 5-15 km long and 2-5 km wide. These streaks are more prominent and intense over the ocean than over land and are near the model's smallest resolvable scale in their widths. These streaks are caused by misovortices at low levels in the PBL and will be discussed in more detail in section 5h. Similar streaks are not possible in the observational analysis because the data are sparse and smoothed. It is an open question whether streaks would be revealed if the observations were as dense in space and time as the model output.

Overall, the MYJ and YSU BULK simulations (Figs. 15b,c) compare most favorably with the analyzed wind swath. The minimum near Miami is approximately 25 m s<sup>-1</sup> and the simulations depict stronger coastal winds, consistent with the observations. The BEP simulations (Figs. 15d,e) capture the broad west-east gradient well, but have winds that are weaker than the analysis in the Miami metropolitan area. Both the MYJ BEP and YSU BEP simulated winds range from 18 to 25 m s<sup>-1</sup>. The BEP and BULK simulations have strong winds right along the coastline, broadly consistent with the observational analysis. It is likely that observational analysis procedures blend the large coastal wind speeds too far inward to the urban corridor. Although the urban winds are too low in comparison to the observational analysis, the BEP simulations have realistic depictions of how strong onshore winds can be reduced by a built-up area. With limited urban stations with which to evaluate the BEP simulations, it is difficult to ascertain how accurate the simulations are in the urban area. As discussed previously, the BEP drag force results from both horizontal and vertical surfaces in the urban environment. Vertical surfaces induce the most drag. To understand the sensitivity of the BEP winds to drag, we reduced the default

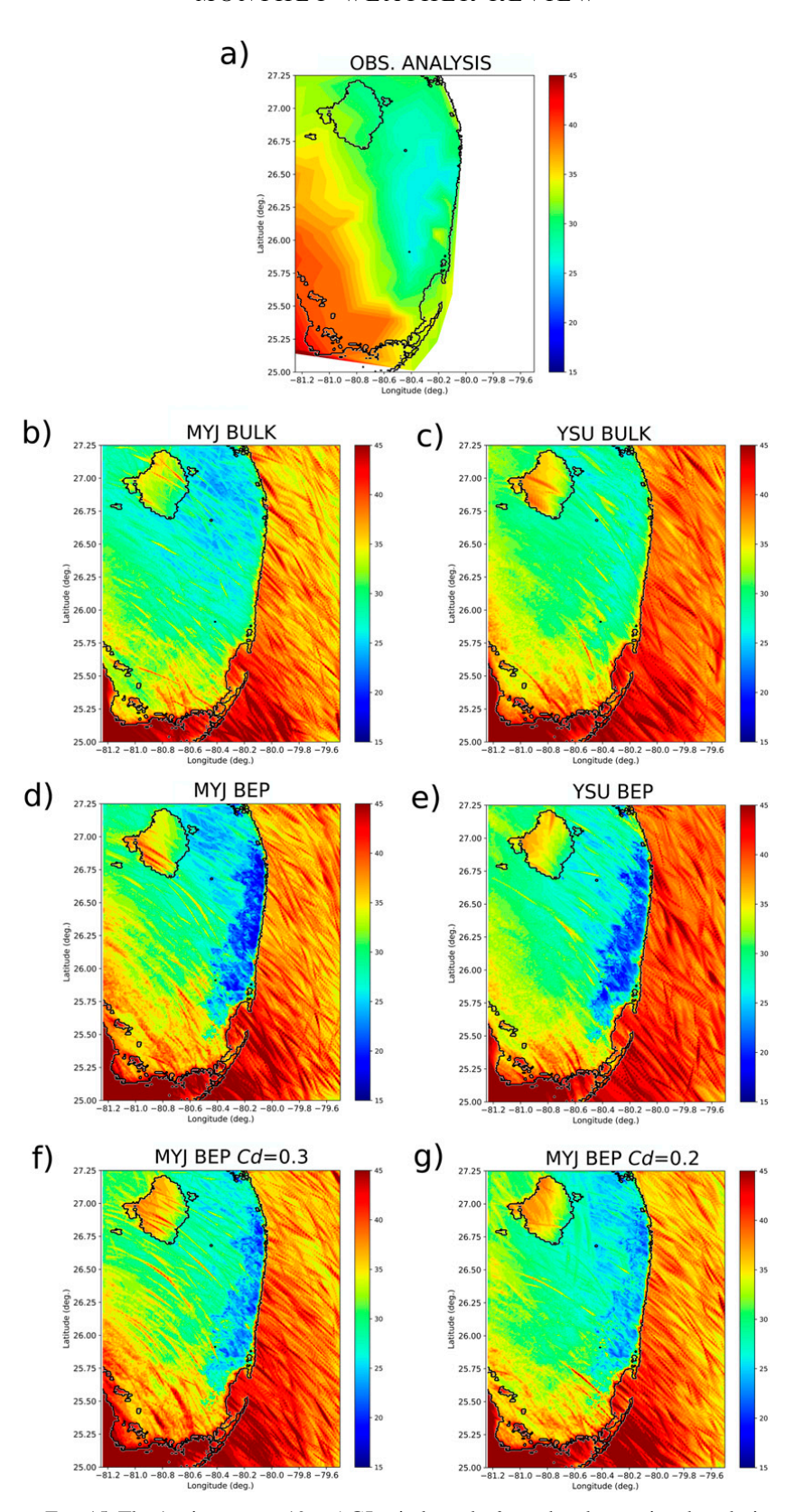


FIG. 15. The 1-min average 10 m AGL wind swaths from the observational analysis and WRF Model simulations: (a) observational analysis of Hagen et al. (2018), (b) MYJ BULK, (c) YSU BULK, (d) MYJ BEP, (e) YSU BEP, (f) MYJ BEP with  $C_d$  = 0.3, and (g) MYJ BEP with  $C_d$  = 0.2. For the simulations, the 20-s output of domain 4 is averaged to 1 min in order to compare to the observations.

drag coefficient of  $C_d = 0.4$  to 0.3 and 0.2, and reran the MYJ BEP simulation for each value. After reducing the drag force in BEP, the simulated MYJ BEP swaths compare more favorably to the observational analysis (Figs. 15f,g). Similar results are obtained by reducing the drag coefficient in BEP in the YSU PBL scheme (not shown).

To quantify the wind swath evaluation, in Fig. 16, scatterplots are shown depicting the model simulated values versus the observational analysis of Hagen et al. (2018). The overall linear correlations are good among all simulations, with Pearson R values between 0.83 and 0.86. In addition to the total values, the statistical performance measures are stratified by urban (land-use category greater than or equal to 31) and rural areas, and are shown on each scatterplot. The MYJ BULK and YSU BULK simulations (Figs. 16a,b) perform the best overall with RMSEs around 4.3-4.9 m s<sup>-1</sup> and biases from 0.5 to 2.4 m s<sup>-1</sup>. They are also superior in the urban environment, with RMSEs of 1.3–2.8 m s<sup>-1</sup> and biases from -2.5 to 0.0 m s<sup>-1</sup>. The MYJ BEP and YSU BEP simulations (Figs. 16c,d) have larger RMSEs than the corresponding bulk simulations overall (5-6 m s<sup>-1</sup>). Biases and RMSEs for BEP in the urban environment are much higher than in the BULK simulations. Biases range from -4.5 to -5.8 m s<sup>-1</sup> and RMSEs range from 7.5 to  $7.7 \,\mathrm{m\,s^{-1}}$ . Finally, examining the MYJ BEP simulations with reduced drag coefficients (Figs. 16e,f), the MYJ BEP simulation with  $C_d = 0.2$  is superior to the simulation with  $C_d =$ 0.3. However, even the  $C_d = 0.2$  simulation does not compare as favorably to the observational analysis as does the MYJ BULK simulation.

#### h. Analysis and discussion of small-scale wind streaks

As mentioned in section 5g, the simulated wind swaths reveal streaks of high wind. To determine the cause of these streaks, we examine details of the simulated boundary layer at the time of peak winds in Miami (1800 UTC 10 September). The relative vertical vorticity at z = 535.7 m on domain 4 is plotted in Fig. 17a. There are multiple cyclonic/anticyclonic vorticity dipoles. Over the ocean, trains of these dipoles exist in rainy regions. There are local instantaneous wind speed maxima at 10 m AGL (Fig. 17b) associated with these dipoles, particularly evident over the ocean. The 1-min sustained wind swaths at 10 m AGL during the previous 5 and 20 min (Figs. 17c,d) show numerous small-scale wind streaks. In particular, there are strong wind streaks over the ocean associated with these anomalies. We will demonstrate that some example wind streaks are caused by misovortices in the HBL (solid and dashed black boxes). The instantaneous wind speed (Fig. 17b) also shows elongated maxima oriented parallel to the flow in southwestern Florida, closer to the center of circulation. It is unclear whether these maxima are caused by misovortices as the wind streaks are, and it is possible that they could be related to other boundary layer coherent structures, such as roll vortices (Morrison et al. 2005).

In Fig. 18, we show an ocean misovortex and associated wind streak. The horizontal scale of the feature is approximately 5 km. At z = 535.7 m, the anomaly contains peak updrafts of  $18 \,\mathrm{m \, s^{-1}}$  collocated with extreme vertical vorticity of  $0.03 \,\mathrm{s^{-1}}$ . A local wind speed maximum exists at the edge of the cyclonic

vorticity anomaly with peak winds of  $66 \,\mathrm{m\,s^{-1}}$ , or approximately  $16 \,\mathrm{m\,s^{-1}}$  higher than the background wind there. Near the surface (Fig. 18b), the local wind maximum is  $42 \,\mathrm{m\,s^{-1}}$ ,  $12 \,\mathrm{m\,s^{-1}}$  higher than the background wind there. The vertical cross section (Fig. 18c) depicts a vertically coherent structure that tilts toward the highest wind speeds ( $z = 0.5 - 2 \,\mathrm{km}$ ). The wind speed and vorticity are maximized at approximately  $z = 1 \,\mathrm{km}$ . Finally, in Fig. 18d, the wind streak caused by this misovortex is shown at  $10 \,\mathrm{m\,AGL}$ . The streak has a horizontal scale of approximately  $5 \,\mathrm{km}$  and a peak 1-min sustained wind speed that is  $40 \,\mathrm{m\,s^{-1}}$ ,  $8 \,\mathrm{m\,s^{-1}}$  higher than the background flow. Since the winds are southerly, the wind streak is oriented in a north–south direction, and located directly behind the misovortex, which is moving to the north.

In Fig. 19, we show two misovortices and associated wind streaks in the urban environment. These simulated misovortices pass over the Fort Lauderdale and Hollywood area. At z = 535.7 m, the anomalies contain peak updrafts of approximately 3 m s<sup>-1</sup> collocated with relative vertical vorticity of approximately 0.01 s<sup>-1</sup>. A local wind speed maximum exists at the edges of the cyclonic vorticity anomalies with peak winds of 54 m s<sup>-1</sup>, approximately 8 m s<sup>-1</sup> higher than the background wind there. Near the surface (Fig. 19b), the local wind maxima are  $30-34 \,\mathrm{m \, s}^{-1}$ , approximately  $4-8 \,\mathrm{m \, s}^{-1}$ higher than the background wind there. The vertical cross sections depict vertically coherent structures, similar to the structures over the ocean, but significantly weaker and more disorganized. The wind streaks (Fig. 19d) are oriented from the southeast to northwest, in the direction of the low-level flow in Figs. 19a and 19b. The 1-min sustained wind streak at 10 m AGL of the southern misovortex has winds of 28- $34 \,\mathrm{m \, s}^{-1}$ ,  $3-9 \,\mathrm{m \, s}^{-1}$  above the background values, and the magnitude decreases rapidly moving inward from the ocean into the urban environment. The 1-min sustained wind streaks at 10 m AGL of the northern misovortex has winds of 28–32 m s<sup>-1</sup>, 3–7 m s<sup>-1</sup> above the background values, and also decreases rapidly moving inland.

These anomalies are consistent with the concept of misovortices that have been examined in other studies (Aberson et al. 2006; Nolan et al. 2009b; Marks et al. 2008; Wurman and Kosiba 2018; Nolan et al. 2021b). Observations indicate that these features are often 1 km or less in horizontal scale (e.g., Marks et al. 2008). The model simulations are producing similar features at their finest resolvable scales of 3-4 km. The large relative vertical vorticity, and spatial orientation of the updrafts, vertical vorticity, and tangential velocity in the misovortices simulated herein are qualitatively similar to these past studies. Marks et al. (2008) reported an eyewall vorticity maximum associated with a misovortex with wind speeds approximately 19 m s<sup>-1</sup> greater than the hurricane vortex peak tangential winds. The simulated misovortex winds over the ocean in Fig. 17 are approximately  $16\,\mathrm{m\,s^{-1}}$  above the background flow, both at z = 535.7 m and z = 26.5 m. Wurman and Kosiba (2018) found both mesovortices with horizontal scales of 2-11 km and tornado-scale vortices with horizontal scales of less than 1 km in the eyewall of landfalling Hurricane Harvey (2017). They found wind speed perturbations of 10-20 m s<sup>-1</sup> above the local background flow in these vortices.

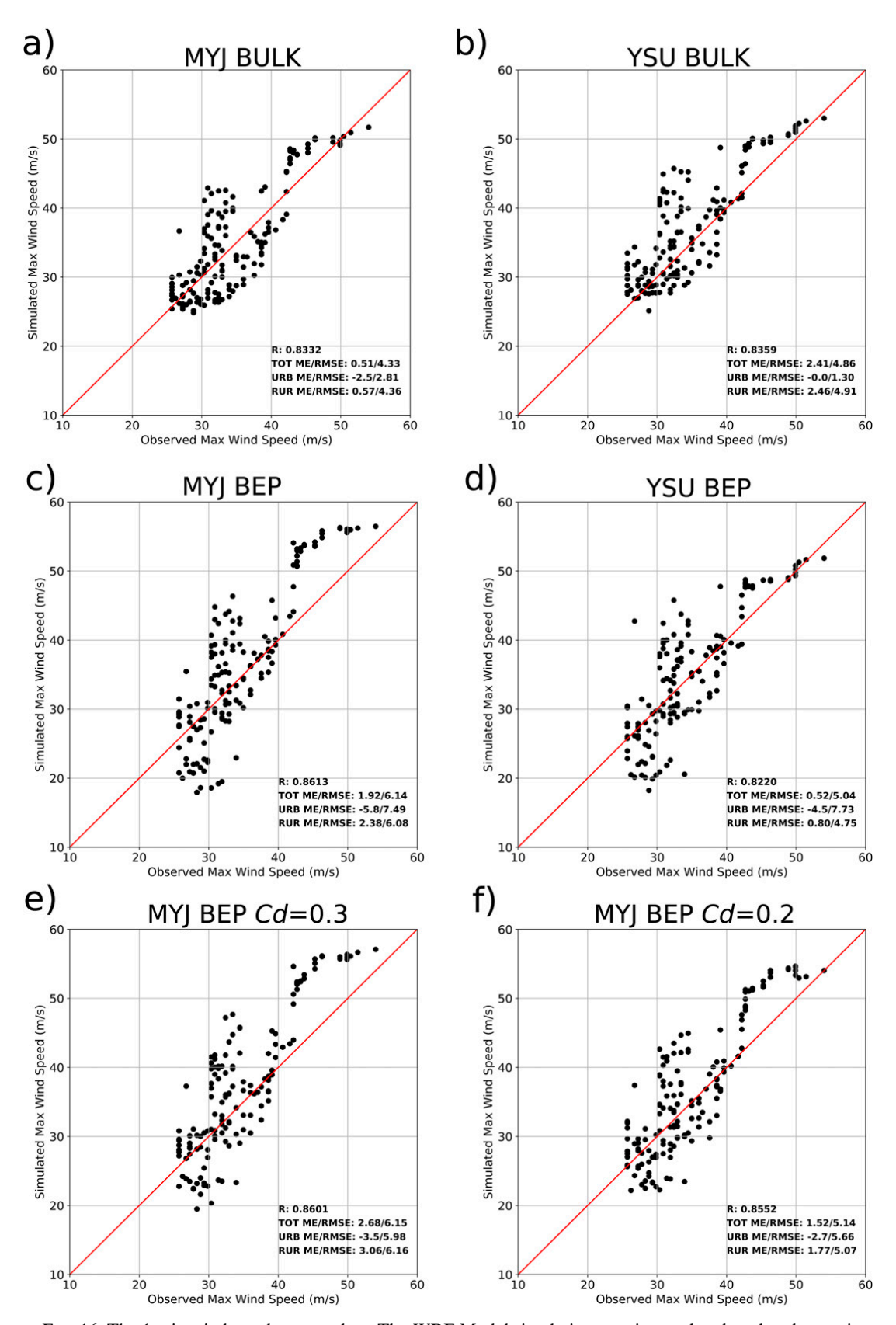


FIG. 16. The 1-min wind swath scatterplots. The WRF Model simulations are interpolated to the observation locations using inverse distance weighting from the nearest four model grid points: (a) MYJ BULK, (b) YSU BULK, (c) MYJ BEP, (d) YSU BEP, (e) MYJ BEP with  $C_d = 0.3$ , and (f) MYJ BEP with  $C_d = 0.2$ . The red diagonal line represents where the simulation exactly equals the measurements. In each panel, the correlation coefficient (R), and total (TOT), urban (URB), and (RUR) mean error and biases are shown.

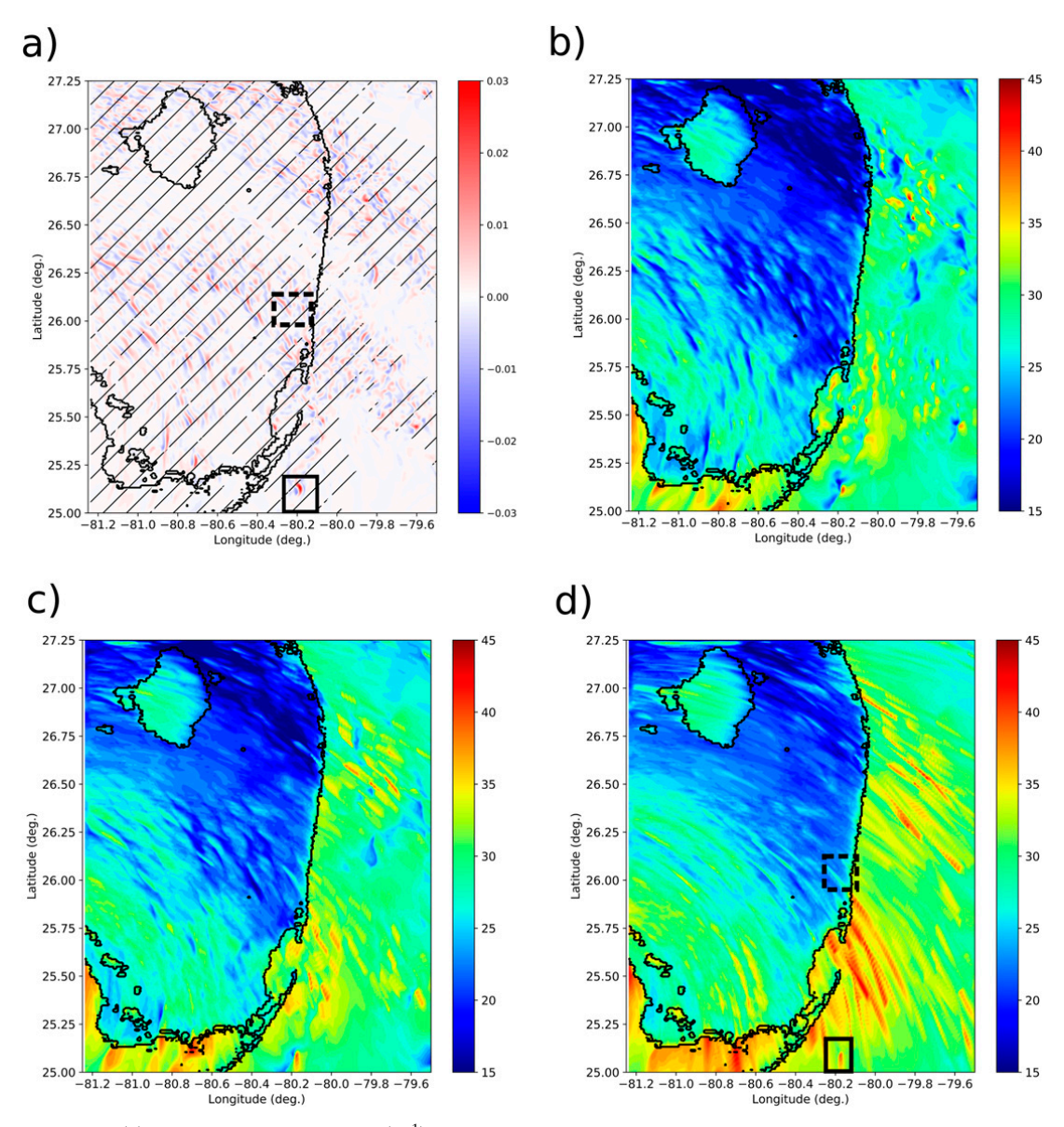


FIG. 17. (a) Relative vertical vorticity ( $s^{-1}$ ) at z=535.7 m at 1800 UTC 10 Sep. Hatched areas denote rainwater mixing ratios greater than zero, (b) instantaneous wind speed (m s<sup>-1</sup>) at 10 m AGL at 1800 UTC 10 Sep, (c) 1-min sustained wind swath (m s<sup>-1</sup>) at 10 m AGL from 1755 to 1800 UTC 10 Sep (prior 5 min), and (d) 1-min sustained wind swath (m s<sup>-1</sup>) at 10 m AGL from 1740 to 1800 UTC 10 Sep (prior 20 min). In (a), an ocean misovortex is identified by the solid-line square, and land misovortices are identified by the dashed-line square for subsequent detailed analysis. In (d), the small-scale wind streaks caused by these misovortices are identified by the same squares. Simulation output is from the MYJ BULK simulation, and the overland values are corrected to open exposure (6).

While the previous work has shown these misovortices exist in the eyewall region, the simulations herein and by Nolan et al. (2021b) suggest that they may also be prominent features in the outer wind field of landfalling tropical cyclones. Considering the extreme winds with these features, they could cause significant localized damage at landfall. Further examination of radar observations of landfalling tropical cyclones could help clarify whether the model simulations are consistent with reality. As anecdotal observational evidence, Hagen et al. (2018) did note small-scale vortex signatures in

the Miami radar's radial velocity field in the same area near the same time (at 1736 UTC 10 September).

# Simulated boundary layer wind reductions in the coastal environment

Finally, we examine how the boundary layer winds are reduced near the surface in the coastal environment of Miami at the time of peak winds. In Fig. 20a, we show  $F = |\mathbf{u}_{10\text{m}}|/|\mathbf{u}_{535.7\text{m}}|$ , wherein  $\mathbf{u}_{10\text{m}}$  is the 10-m diagnosed horizontal wind vector and  $\mathbf{u}_{535.7\text{m}}$  is the model's horizontal wind vector at 535.7 m.

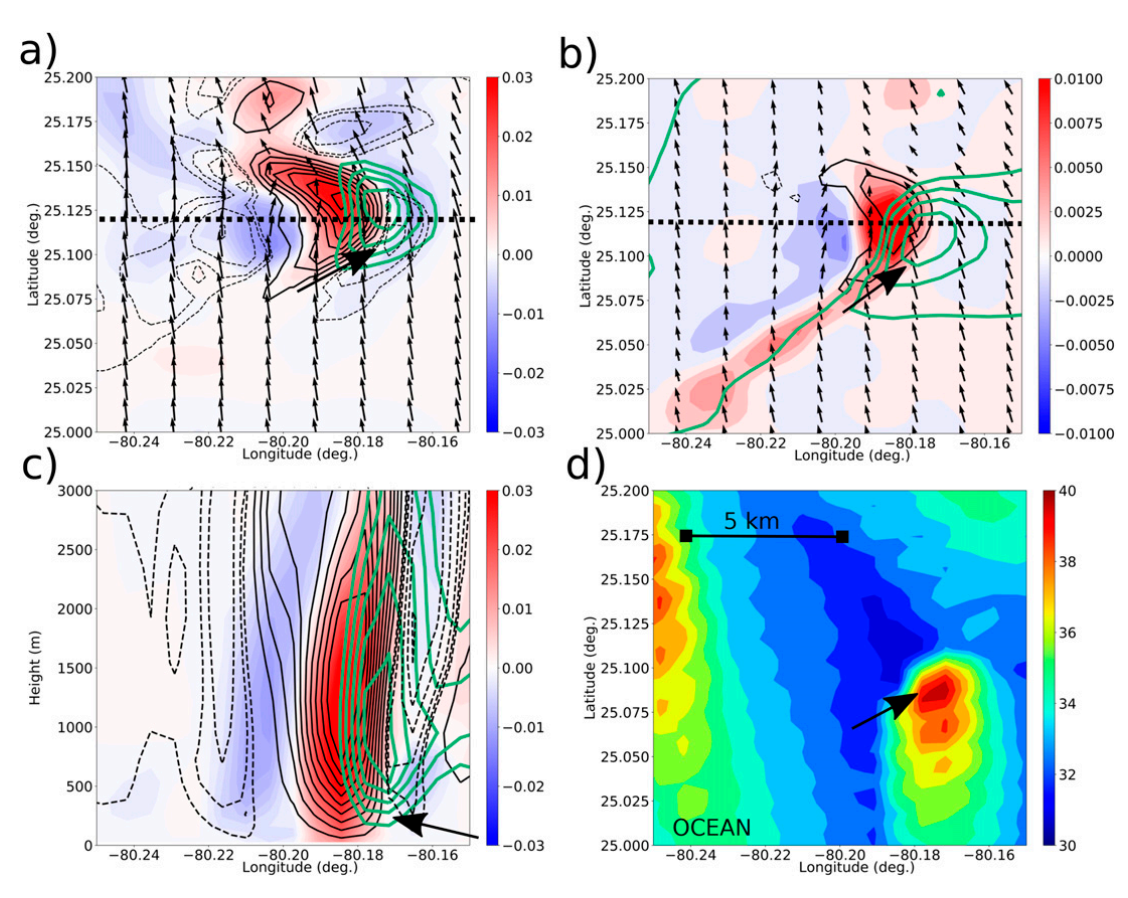


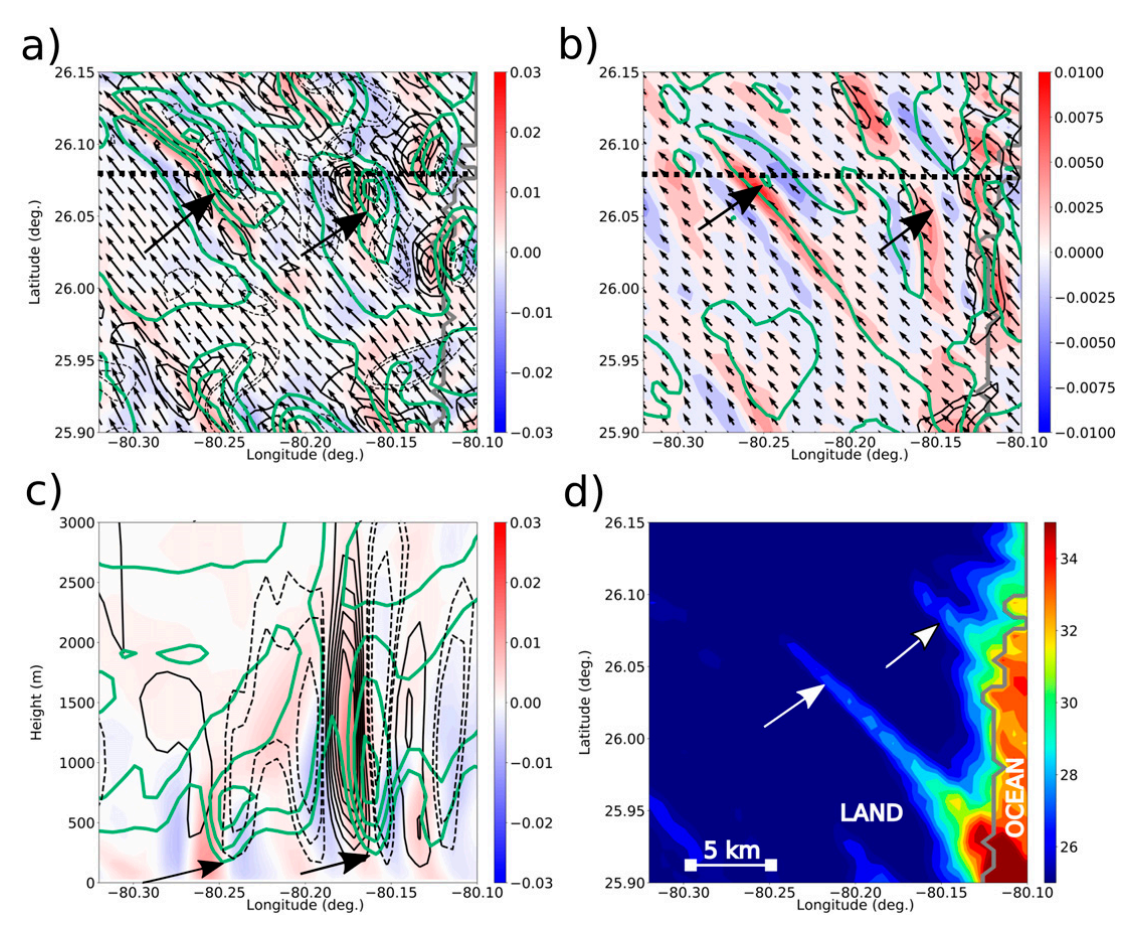
FIG. 18. Detailed analysis of the ocean misovortex in Fig. 17 in the MYJ BULK simulation: (a) relative vertical vorticity ( $\rm s^{-1}$ ), vertical velocity ( $\rm m \, s^{-1}$ ; black contours), and horizontal velocity anomaly ( $\rm m \, s^{-1}$ ; thick sea green contours) at  $z=535.7\,\rm m$ ; (b) relative vertical vorticity ( $\rm s^{-1}$ ), vertical velocity ( $\rm m \, s^{-1}$ ), and horizontal velocity anomaly ( $\rm m \, s^{-1}$ ) at  $z=25.7\,\rm m$ ; (c) cross section of relative vertical vorticity ( $\rm s^{-1}$ ), vertical velocity ( $\rm m \, s^{-1}$ ), and horizontal velocity anomaly ( $\rm m \, s^{-1}$ ) at a latitude of 25.1277° [dotted line in (a) and (b)]; and (d) 1-min sustained wind swath ( $\rm m \, s^{-1}$ ) at 10 m AGL from 1740 to 1800 UTC 10 Sep (prior 20 min). In (a) and (c), the vertical velocity contour levels are -8, -6, -4, -2, 2, 4, 6, 8, 10, 12, 14, 16, and 18, and the horizontal velocity anomaly contour levels are 50, 54, 58, 62, and 66. In (b), the vertical velocity contour levels are -0.25, 0.25, and 0.5, and the horizontal velocity anomaly contour levels are 30, 34, 38, and 42. Negative vertical velocities are marked with dashed contours. Arrows are used to identify the wind maxima of the misovortices and associated wind streaks.

Lower values of F denote more reductions in winds. Over the ocean in the MYJ BULK and MYJ BEP simulations, F = 0.6-0.8. In the YSU BULK and BEP simulations, F = 0.7 - 0.85. Over land in rural areas, F = 0.4 in the MYJ BULK simulation and F = 0.5 in the YSU BULK simulation. The MYJ BULK simulation winds also are reduced more than the YSU BULK simulation winds in the urban area. The MYJ BEP and YSU BEP simulation reductions in the urban area are similar (F = 0.3-0.4) and smaller than the BULK simulations. Smaller F in the BEP simulations at the time of peak winds indicate that the boundary layer winds are reduced dramatically near the the surface. As an example, a peak wind of  $50 \,\mathrm{m \, s^{-1}}$  at  $z = 535.7 \,\mathrm{m}$  would be reduced to  $15-20 \,\mathrm{m \, s^{-1}}$  at  $z=10 \,\mathrm{m}$ . The reduction F derived from assuming a logarithmic profile moving downward from  $z = 535.7 \,\mathrm{m}$  over land, and an ocean value based upon Franklin et al. (2003) (Fig. 20b) are reasonably similar to the WRF simulations in Fig. 20a. In particular, the logarithmic assumption fraction compares most favorably with both

YSU simulations. The MYJ fractions F are slightly lower than those from Fig. 20b over rural areas and over the ocean. The results indicate that a neutral condition assumption can be used to a first approximation to reduce the  $z=535.7\,\mathrm{m}$  outer winds to  $z=10\,\mathrm{m}$  at the time of peak winds in Miami for this case study.

# 6. Conclusions

We evaluated four WRF Model simulations with configurations comprising two very different PBL (MYJ and YSU) and urban canopy (BULK and BEP) parameterizations against near-surface observations as the outer wind field of Hurricane Irma (2017) interacted with Miami. To resolve fine-scale details of the wind in urban areas, a fourth domain with horizontal grid spacing of  $\Delta x = 0.67 \, \mathrm{km}$  was placed over the Miami metropolitan area. The simulated urban near-surface winds were weakly sensitive to the PBL scheme and strongly sensitive to the UCM. Simulations



using a simple bulk scheme were the ones that produced wind speeds most similar to observations at airports on the edges of urban environments (biases ranging from -2 to  $2\,\mathrm{m\,s^{-1}}$ ). In contrast, the multilayer BEP simulations had winds that were negatively biased, from approximately -2 to  $-6\,\mathrm{m\,s^{-1}}$  on average. Compared to an observational wind swath analysis (peak 1-min sustained wind over the duration of the landfall at a point), biases in the urban environment were from 0.0 to  $-2.5\,\mathrm{m\,s^{-1}}$  in the BULK simulations and from -4.5 to  $-5.8\,\mathrm{m\,s^{-1}}$  in the BEP simulations. Biases in the rural environment against the analyzed wind swath were similar among the bulk and BEP simulations, and ranged from +0.5 to  $+2.4\,\mathrm{m\,s^{-1}}$ . The biases and errors were generally similar in both the MYJ BEP and YSU BEP simulations.

The urban wind biases were improved by reducing the drag coefficient in BEP, indicating that the default drag coefficient in BEP may need to be reduced in higher wind conditions, but further study is needed. In particular, the wind swath observational analysis is dominated by measurements in openly exposed areas, and thus might not accurately represent the urban winds. Indeed, the BEP simulations performed best compared to the reduced WSUMH observations amidst buildings in downtown Miami.

The similarities of BEP's behavior in both the MYJ and YSU PBL schemes are consistent with the modeling study by Hendricks et al. (2020) that examined simulations of simpler, more typical synoptic conditions. This indicates that the BEP's urban surface sources are dominant over the vertical mixing effect in forcing state variables near the surface. The simulated TKE in the MYJ BEP simulation matched the observational TKE estimates in the Miami metropolitan area better than the MYJ BULK simulation, which was biased high. A plausible explanation for BEP's superior performance is the increased near-surface urban

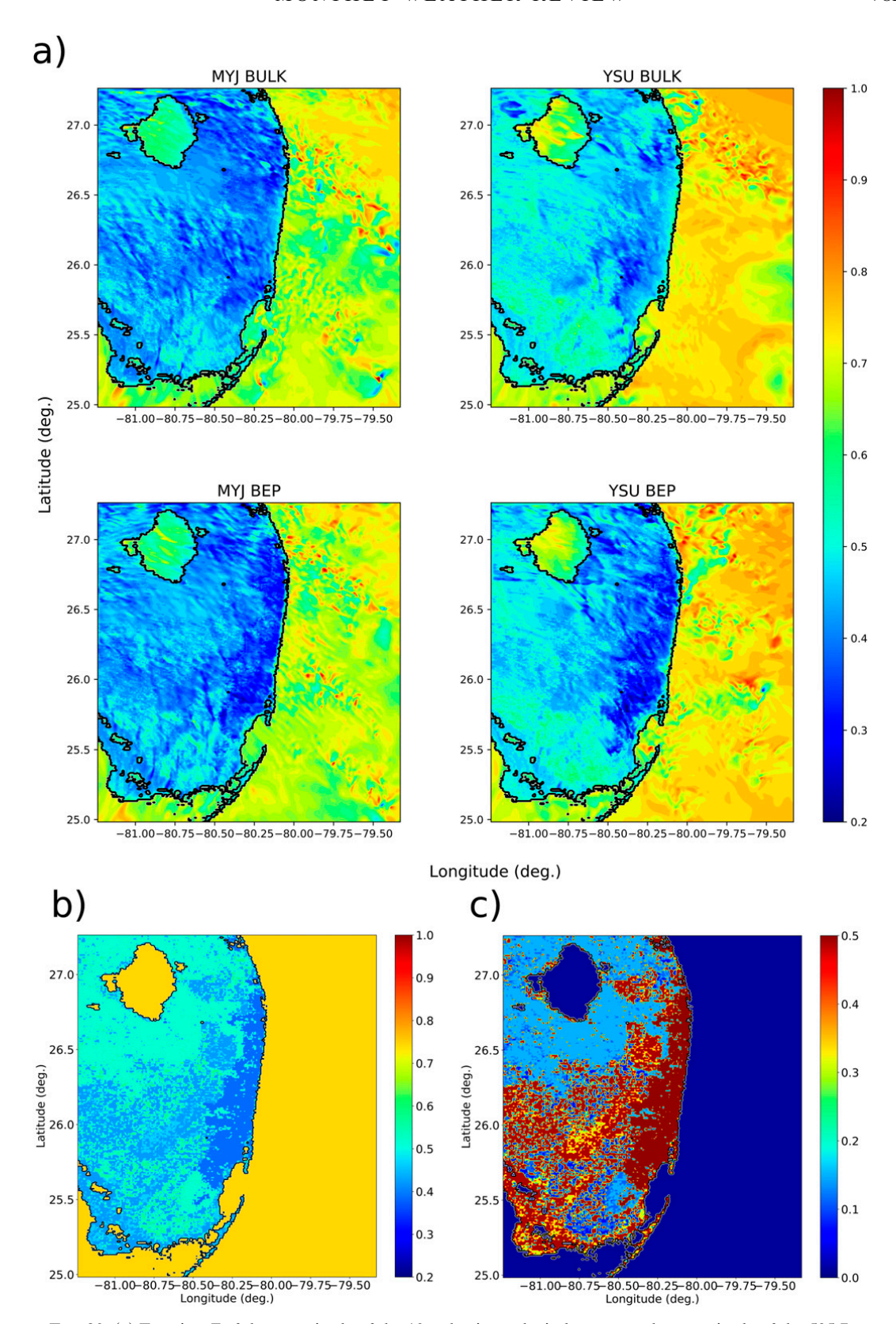


FIG. 20. (a) Fraction F of the magnitude of the 10-m horizontal wind vector to the magnitude of the 535.7-m horizontal wind vector at 1800 UTC 10 Sep in the MYJ BULK, MYJ BEP, YSU BULK, and YSU BEP simulations, (b) F assuming a logarithmic profile downward from z = 535.7 m to compute the 10-m wind speed using the WRF surface roughness over land and F = 0.75 over the ocean and lakes based on the outer wind field composite of Franklin et al. (2003), and (c) surface roughness length (m).

TKE dissipation through a reduction in the turbulence length scales due to buildings.

We have shown the usefulness of high-resolution numerical simulations with the multilayer BEP in predicting realistic heterogeneous wind structures in the urban environment as the outer wind field of a hurricane interacted with Miami. Dramatic ocean-to-urban wind reductions were simulated with BEP from  $30-40 \,\mathrm{m\,s^{-1}}$  just off the coast to  $15-25 \,\mathrm{m\,s^{-1}}$ inland 1-2 km from the coast. Dense observations from urban microscale networks during hurricane landfalls could help clarify whether such dramatic wind reductions happen in reality. This information would be of critical importance for wind hazard mitigation in cities. To our knowledge, these simulations are the first examination of BEP's performance modeling a hurricane landfall. They point the way toward improvements that can be made to BEP for simulating the interaction between high winds and built-up environments. More generally, our findings are a reminder than it is useful to evaluate and improve parameterization schemes' ability to simulate rare, yet extremely consequential weather, for which they might not be optimized.

In closing, we wish to note a few important limitations of this study. One limitation is the temporal and spatial sparseness of the observations, which did not permit us to verify that small-scale features in the model simulations (e.g., misovortices) existed in reality. Second, the WRF simulations are too coarse to resolve some important small-scale features in the PBL below their effective horizontal resolutions of 3–4 km. Among these features are boundary layer roll vortices (Foster 2005; Morrison et al. 2005). A final limitation of the current study is that the peak inflow winds in Miami were at minimal hurricane force (35 m s<sup>-1</sup>). In the future, it would be useful to examine how well BEP performs in a scenario where the eyewall of a major hurricane (maximum winds greater than 49 m s<sup>-1</sup>) makes a direct landfall in a city. Such analysis could lead to further improvements in BEP for simulating extreme wind conditions.

Acknowledgments. This material is based upon work supported by the National Center for Atmospheric Research (NCAR), which is a major facility sponsored by the National Science Foundation under Cooperative Agreement 1852977. The authors acknowledge the support from the National Science Foundation (NSF) Prediction of and Resilience against Extreme Events (PREEVENTS) Grant 1663978, managed by Justin E. Lawrence. We thank Andrew Hagen of NOAA/NHC for providing the observational wind swath analysis data and John Knaff of NOAA/RAMMB for providing the tropical cyclone surface wind analysis data. We thank Brian McNoldy, Yi Wang, George Bryan, Forrest Masters, Pedro Fernández-Cabán, and Alberto Martilli for helpful discussions. We thank Ed Mansouri for providing the specifications of the WeatherStem instruments. This manuscript was improved by the constructive comments of two anonymous reviewers.

*Data availability statement.* Observational data and model simulations used in this study are accessible online at https://doi.org/10.5065/86q5-hh48.

### APPENDIX A

# Description of Numerical Solutions to Diffusion Equations with BEP Sources

Equations (4) and (5) are solved using implicit–explicit time differencing: the diffusion term is treated implicitly, and the source term can be treated either implicitly, explicitly, or split between the two. In both the YSU and MYJ PBL parameterizations, the rural heat and moisture flux divergences at the surface are treated explicitly. The rural values are  $B_{\theta,\text{rur}} =$  $\text{HFX}/(\rho c_p \Delta z)$  and  $B_{q_v,\text{rur}} = \text{QFX}/(\rho \Delta z)$ , wherein  $B_{\theta,\text{rur}}$  is the explicit rural potential temperature source,  $B_{q_n,rur}$  is the explicit rural moisture source, HFX is the rural upward sensible heat flux, QFX is the rural upward moisture flux,  $\rho$  is the density,  $\Delta z$  is the vertical grid spacing at the lowest model level, and the subscript rur denotes rural fluxes. The corresponding rural implicit sources  $A_{\theta,\text{rur}} = A_{q_v,\text{rur}} = 0$ . The urban heat fluxes are all explicit (Martilli et al. 2009). In the MYJ and YSU PBL parameterizations, the rural momentum sources are treated implicitly, i.e.,  $B_{u,\text{rur}} = 0$  and  $B_{v,\text{rur}} = 0$  and  $A_{u,\text{rur}} = A_{v,\text{rur}} = -u_*^2/(\sqrt{u^2 + v^2} \Delta z)$ , wherein  $A_{u,\text{rur}}$  and  $A_{v,\text{rur}}$ are the implicit surface rural zonal and meridional momentum sources, respectively. The vertical surface (building wall) urban momentum source term is split between the implicit  $(A_{u,urb}, A_{v,urb})$  and explicit  $(B_{u,urb}, B_{v,urb})$  components (Martilli et al. 2009). For urban horizontal surfaces (roofs and roads), the momentum forcing is in the explicit B components. Because the WRF Model uses second-order accurate vertical differencing for the MYJ and YSU diffusion equations, the discrete versions of (4) and (5) reduce to tridiagonal matrix problems. In the discrete linear problems, the A components are placed in the tridiagonal matrix and the B components are placed in the explicit source term vectors.

#### APPENDIX B

# Observations and Procedures Used in the Wind Swath Analysis

Here, we provide more details on the Hagen et al. (2018) analysis. The following surface networks are used: ASOS, WeatherBug, WxFlow, NDBC, National Ocean Service (NOS), Remote Automated Weather Stations (RAWS), Florida Automated Weather Network (FAWN), Citizen Weather Observing Program (CWOP), South Florida Water Management District (SFWMD), Soil Climate Analysis Network (SCAN), WeatherStem, Integrated Coral Observing Network (ICON), personal weather stations, and an anemometer from a spotter. There are a total of 75 stations. All observations are converted to a maximum 1-min sustained wind at 10 m AGL. For converting elevated anemometers to 10 m, the Franklin et al. (2000) curve is used. For anemometers below 10 m, the power law relation of Hsu et al. (1994) is used to adjust the winds to 10 m. To convert the time-average of the observation to a 1-min average, the factors used are 1.03, 1.06, 1.12, and 1.13, for 2-, 5-, 10-, and 15-min average winds, respectively.

TABLE B1. Reduction factors used to convert radar velocities to 10 m AGL (Hagen et al. 2018). The reduction factors are based upon Franklin et al. (2003).

Height (m)	Eyewall	Outer convection	Outer nonconvection
3048	0.90	0.85	0.80
1524	0.80	0.80	0.75
762	0.75	0.75	0.75
304.8	0.80	0.80	0.80
152.4	0.80	0.80	0.80

The radar data used are from the WSR-88D radar from Miami, Florida (KAMX). The Franklin et al. (2003) methodology is used to reduce winds from a given altitude to 10 m. The radar is first compared to 32 reliable maximum wind observations. The pixels (or radar sample volumes) within a radial distance of 8–16 km and 5–10 min of a point are averaged. The lower tilts are used, and no radar data above 3048 m is used. The reduction factors for the radar are given in Table B1. The radar data on average are 3.6 m s<sup>-1</sup> higher than the anemometer data, and thus the data are bias-corrected. In the final analysis, the anemometer data are weighted heavily in areas with good coverage of reliable winds. In areas with questionable anemometer data, a combination of the radar data and anemometer data are used. In areas without anemometer data, the bias-corrected radar data are used (reduction of 3.6 m s<sup>-1</sup>).

#### APPENDIX C

# **Procedure Used to Estimate TKE from Gust Factors**

Observational estimates of TKE are calculated using a direct and an empirical method. In the direct method, turbulent perturbations are computed as the difference between the peak gust (or peak 5-s mean during the 2-min period) (Powell 1993) and the 2-min mean wind every minute directly from the ASOS measurements (Masters et al. 2010a). The TKE is computed as

TKE(t) = 
$$\frac{u'(t)^2 + v'(t)^2 + w'(t)^2}{2}$$
, (C1)

wherein u(t) is the gust zonal velocity, v(t) is the gust meridional velocity, and w(t) is the gust vertical velocity. The turbulent perturbations for zonal and meridional velocity are computed as  $u'(t) = u(t) - \overline{u}(t)$  and  $v'(t) = v(t) - \overline{v}(t)$ , wherein  $\overline{u}(t)$ ,  $\overline{v}(t)$  are the 2-min mean values from ASOS. Since ASOS does not measure vertical velocity, we assume isotropy to compute w'(t). This assumption likely leads to a slight overestimate of the TKE because w'(t) is typically estimated to be smaller than both u'(t) and v'(t) (Masters et al. 2010b).

In the empirical method, we use the the linear curve fits of Masters et al. (2010b) that relate gust factors to turbulence intensity (their Figs. 10 and 11, respectively). The Masters et al. (2010b) empirical curves were developed from 10-Hz tower observations of the landfalling hurricanes of Katrina, Rita, and Wilma (2005 storms) at  $5-10 \,\mathrm{m}$  AGL. The sequential procedure used in the empirical method is as follows. Let U(t) be the

ASOS horizontal along-streamflow,  $U_{5\rm sec}(t)$  be the ASOS gust wind speed,  $U_{2\min}(t)$  be the ASOS mean wind speed, and  $GF_a(t) = U_{5sec}(t)/U_{2min}(t)$  be the ASOS gust factor. First, the 5s gust of ASOS is assumed to be equivalent to the 3-s gust of Masters et al. (2010b). Second, the 2-min mean wind speed of ASOS is converted to a 15-min mean wind speed, which was used by Masters et al. (2010b). Letting  $U_{15\text{min}}$  be the 15-min wind speed, this is accomplished through  $U_{15\min} = U_{2\min}(t)/1.13$  based upon Harper et al. (2010), or equivalently  $GF_m(t) = 1.13GF_a(t)$ , wherein  $GF_m(t)$  is the equivalent gust factor based upon 15min mean winds. Third, Masters et al.'s (2010b) Figs. 10 and 11 linear curve fits are used to estimate the turbulence intensity from the gust factors. Masters et al. (2010b) empirically showed that there is a linear relationship between gust factors and turbulence intensity, with higher gust factors corresponding to larger turbulence intensities. The linear equation based on their empirical data is

$$\sigma_{u}(t) = 0.01U(t)[GF_{m}(t) - B]/A,$$
 (C2)

wherein  $\sigma_u(t)$  is the along-stream turbulence intensity, and A, B are constants. Two curve fits are used: EMP1 [Fig. 10 of Masters et al. (2010b), all storms] with A,  $B = 0.036\,09$ , 0.8824; and EMP2 (Fig. 11 of Masters et al. (2010b), Hurricane Rita (2005) only) with A, B = 0.0244, 1.118. Fourth, the crossstream and vertical turbulence intensities are calculated based upon the average relationships described on page 535 of Masters et al. (2010b):  $\sigma_v(t) = 0.738\,09\sigma_u(t)$  (12.4/16.8) and  $\sigma_w(t) = 0.404\,76\sigma_u(t)$  (6.8/16.8). These relationships of the cross-stream and vertical components to the along-stream component are also similar to the results of Miller et al. (2015). Finally the TKE is calculated as

TKE(t) = 
$$\frac{\sigma_u(t)^2 + \sigma_v(t)^2 + \sigma_w(t)^2}{2}$$
. (C3)

### REFERENCES

Abarca, S. F., M. T. Montgomery, and J. C. McWilliams, 2015: The azimuthally-averaged boundary layer structure of a numerically simulated major hurricane. *J. Adv. Model. Earth Syst.*, 7, 1207–1219, https://doi.org/10.1002/2015MS000457.

Aberson, S. D., M. Montgomery, M. Bell, and M. Black, 2006: Hurricane Isabel (2003)—New insights into the physics of intense storms. Part II: Extreme localized wind. *Bull. Amer. Meteor. Soc.*, 87, 1349–1354, https://doi.org/10.1175/BAMS-87-10-1349.

Alford, A. A., J. A. Zhang, M. I. Biggerstaff, P. Dodge, F. D. Marks, and D. J. Bodine, 2020: Transition of the hurricane boundary layer during the landfall of Hurricane Irene (2011). J. Atmos. Sci., 77, 3509–3531, https://doi.org/10.1175/JAS-D-19-0290.1.

Barnes, G. M., and M. D. Powell, 1995: Evolution of the inflow boundary layer of Hurricane Gilbert (1988). *Mon. Wea. Rev.*, **123**, 2348–2368, https://doi.org/10.1175/1520-0493(1995) 123<2348:EOTIBL>2.0.CO;2.

Braun, S. A., and W.-K. Tao, 2000: Sensitivity of high-resolution simulations of Hurricane Bob (1991) to planetary boundary layer parameterizations. *Mon. Wea. Rev.*, **128**, 3941–3961, https://doi.org/10.1175/1520-0493(2000)129<3941:SOHRSO>2.0.CO;2.

- Bryan, G. H., 2012: Effects of surface exchange coefficients and turbulence length scales on the intensity and structure of numerically simulated hurricanes. *Mon. Wea. Rev.*, **140**, 1125–1143, https://doi.org/10.1175/MWR-D-11-00231.1.
- Bu, Y. P., R. G. Fovell, and K. L. Corbosiero, 2017: The influences of boundary layer mixing and cloud-radiative forcing on tropical cyclone size. *J. Atmos. Sci.*, 74, 1273–1292, https:// doi.org/10.1175/JAS-D-16-0231.1.
- Cangialosi, J. P., A. S. Latto, and R. Berg, 2018: National Hurricane Center Tropical Cyclone Report: Hurricane Irma (30 August– 12 September 2017). Tech. Rep. AL112017, National Hurricane Center, 111 pp., https://www.nhc.noaa.gov/data/tcr/AL112017\_ Irma.pdf.
- Chen, F., and Coauthors, 2011: The integrated WRF/urban modeling system: Development, evaluation, and applications to the urban environmental problems. *Int. J. Climatol.*, 31, 273–288, https://doi.org/10.1002/joc.2158.
- Ching, J., and Coauthors, 2009: National urban database and access portal tool. *Bull. Amer. Meteor. Soc.*, 90, 1157–1168, https://doi.org/10.1175/2009BAMS2675.1.
- Donelan, M. A., B. K. Haus, N. Reul, W. J. Plant, M. Stiassnie, and H. C. Graber, 2004: On the limiting aerodynamic roughness of the ocean in very strong winds. *Geophys. Res. Lett.*, **31**, L18306, https://doi.org/10.1029/2004GL019460.
- Drennan, W. M., J. A. Zhang, J. R. French, C. McCormick, and P. G. Black, 2007: Turbulent fluxes in the hurricane boundary layer. Part II: Latent heat flux. *J. Atmos. Sci.*, **64**, 1103–1115, https://doi.org/10.1175/JAS3889.1.
- Ek, M. B., K. E. Mitchell, Y. Lin, E. Rogers, P. Grummann, G. Gayno, and J. D. Tarpley, 2003: Implementation of Noah land surface model advances in the National Centers for Environmental Prediction operational mesoscale Eta model. J. Geophys. Res., 108, 2002JD003296, https://doi.org/10.1029/ 2002JD003296.
- Fernández-Cabán, P. L., and Coauthors, 2019: Observing Hurricane Harvey's eyewall at landfall. *Bull. Amer. Meteor. Soc.*, **100**, 759–775, https://doi.org/10.1175/BAMS-D-17-0237.1.
- Foster, R. C., 2005: Why rolls are prevalent in the hurricane boundary layer. *J. Atmos. Sci.*, **62**, 2647–2661, https://doi.org/10.1175/JAS3475.1.
- Franklin, J. L., M. L. Black, and K. Valde, 2000: Eyewall wind profiles in hurricanes determined by GPS dropwindsondes. NOAA, accessed 23 March 2021, https://www.nhc.noaa.gov/aboutwindprofile.shtml.
- —, —, and —, 2003: GPS dropwindsonde wind profiles in hurricanes and their operational implications. *Wea. Forecasting*, 18, 32–44, https://doi.org/10.1175/1520-0434(2003)018<0032: GDWPIH>2.0.CO;2.
- French, J. R., W. M. Drennan, J. A. Zhang, and P. G. Black, 2007: Turbulent fluxes in the hurricane boundary layer. Part I: Momentum flux. J. Atmos. Sci., 64, 1089–1102, https://doi.org/ 10.1175/JAS3887.1.
- Guimond, S. R., G. M. Heymsfield, and F. J. Turk, 2010: Multiscale observations of Hurricane Dennis (2005): The effects of hot towers on rapid intensification. *J. Atmos. Sci.*, 67, 633–654, https://doi.org/10.1175/2009JAS3119.1.
- —, J. A. Zhang, J. W. Sapp, and S. J. Frasier, 2018: Coherent turbulence in the boundary layer of Hurricane Rita (2005) during an eyewall replacement cycle. *J. Atmos. Sci.*, **75**, 3071–3093, https://doi.org/10.1175/JAS-D-17-0347.1.
- Hagen, A. B., K. Scharfenberg, A. Moses, S. Konarik, and R. Garcia, 2018: An analysis of Hurricane Irma's maximum winds in south Florida. 33rd Conf. on Hurricanes and Tropical Meteorology, Ponte Vedra, FL, Amer. Meteor. Soc., 68,

- https://ams.confex.com/ams/33HURRICANE/webprogram/Paper339589.html.
- Harper, B. A., J. D. Kepert, and J. D. Ginger, 2010: Guidelines for converting between various wind averaging periods in tropical cyclone conditions. World Meteorological Organization Tech. Rep., 64 pp.
- Haus, B. K., D. Jeong, M. A. Donelan, J. A. Zhang, and I. Savelyev, 2010: Relative rates of sea-air heat transfer and frictional drag in very high winds. *Geophys. Res. Lett.*, 37, L07802, https://doi.org/10.1029/2009GL042206.
- Hendricks, E. A., J. C. Knievel, and Y. Wang, 2020: Addition of multiple layer urban canopy models to a nonlocal planetary boundary layer parameterization and evaluation in ideal and real scenarios. J. Appl. Meteor. Climatol., 59, 1369–1392, https://doi.org/10.1175/JAMC-D-19-0142.1.
- Hirth, B. D., J. L. Schroeder, C. C. Weiss, D. A. Smith, and M. I. Biggerstaff, 2012: Research radar analyses of the internal boundary layer over Cape Canaveral, Florida, during the landfall of Hurricane Frances (2004). Wea. Forecasting, 27, 1349–1372, https://doi.org/10.1175/WAF-D-12-00014.1.
- Hong, S.-Y., Y. Noh, and J. Dudhia, 2006: A new vertical diffusion package with an explicit treatment of entrainment processes. *Mon. Wea. Rev.*, 134, 2318–2341, https://doi.org/10.1175/MWR3199.1.
- Hsu, S. A., E. A. Meindl, and D. B. Gilhousen, 1994: Determining the power-law wind profile exponent under near-neutral stability conditions at sea. J. Appl. Meteor., 33, 757–765, https://doi.org/ 10.1175/1520-0450(1994)033<0757:DTPLWP>2.0.CO;2.
- Iacono, M. J., J. S. Delamere, E. J. Mlawer, M. W. Shephard, S. A. Clough, and W. D. Collins, 2008: Radiative forcing by long-lived greenhouse gases: Calculations with the AER radiative transfer models. *J. Geophys. Res.*, 113, D13103, https://doi.org/10.1029/2008JD009944.
- Ingel, L. K., 2005: On the nonlinear dynamics of the boundary layer of intense atmospheric vortex. *Dyn. Atmos. Oceans*, 40, 295– 304, https://doi.org/10.1016/j.dynatmoce.2005.08.002.
- Janjić, Z. I., 1994: The step mountain Eta coordinate model: Further developments of the convection, viscous sublayer, and turbulence closure schemes. *Mon. Wea. Rev.*, 122, 927–945, https://doi.org/ 10.1175/1520-0493(1994)122<0927:TSMECM>2.0.CO;2.
- Jiménez, P., J. Dudhia, J. F. Gonzalez-Rouco, J. Navarro, J. P. Montávez, and E. García-Bustamante, 2012: A revised scheme for the WRF surface layer formulation. *Mon. Wea. Rev.*, 140, 898–918, https://doi.org/10.1175/MWR-D-11-00056.1.
- Kepert, J. D., 2001: The dynamics of boundary layer jets within the tropical cyclone core. Part I: Linear theory. *J. Atmos. Sci.*, **58**, 2469–2484, https://doi.org/10.1175/1520-0469(2001)058<2469: TDOBLJ>2.0.CO:2.
- —, 2006a: Observed boundary layer wind structure and balance in the hurricane core. Part I: Hurricane Georges. *J. Atmos. Sci.*, **63**, 2169–2193, https://doi.org/10.1175/JAS3745.1.
- ——, 2006b: Observed boundary layer wind structure and balance in the hurricane core. Part II: Hurricane Mitch. *J. Atmos. Sci.*, 63, 2194–2211, https://doi.org/10.1175/JAS3746.1.
- ——, 2017: Time and space scales in the tropical cyclone boundary layer, and the location of the eyewall updraft. *J. Atmos. Sci.*, **74**, 3305–3323, https://doi.org/10.1175/JAS-D-17-0077.1.
- ——, 2018: The boundary layer dynamics of tropical cyclone rainbands. *J. Atmos. Sci.*, **75**, 3777–3795, https://doi.org/10.1175/JAS-D-18-0133.1.
- —, and Y. Wang, 2001: The dynamics of boundary layer jets within the tropical cyclone core. Part II: Nonlinear enhancement. *J. Atmos. Sci.*, **58**, 2485–2501, https://doi.org/10.1175/1520-0469(2001)058<2485:TDOBLJ>2.0.CO;2.

- —, J. Schwendike, and H. Ramsay, 2016: Why is the tropical cyclone boundary layer not "well mixed"? *J. Atmos. Sci.*, 73, 957–973, https://doi.org/10.1175/JAS-D-15-0216.1.
- Klotzbach, P. J., S. G. Bowen, R. Pielke Jr., and M. Bell, 2018: Continental U.S. hurricane landfall frequency and associated damage: Observations and future risks. *Bull. Amer. Meteor. Soc.*, 99, 1359–1376, https://doi.org/10.1175/BAMS-D-17-0184.1.
- Knaff, J. A., S. P. Longmore, R. T. DeMaria, and D. A. Molenar, 2015: Improved tropical-cyclone flight-level wind estimates using routine infrared satellite reconnaissance. *J. Appl. Meteor. Climatol.*, **54**, 463–478, https://doi.org/10.1175/JAMC-D-14-0112.1.
- Kosiba, K. A., and J. Wurman, 2014: Finescale dual-Doppler analysis of hurricane boundary layer structures in Hurricane Frances (2004) at landfall. *Mon. Wea. Rev.*, 142, 1874–1891, https://doi.org/10.1175/MWR-D-13-00178.1.
- ——, F. Masters, and P. Robinson, 2013: Mapping of near-surface winds in Hurricane Rita using fine-scale radar, ane-mometer, and land-use data. *Mon. Wea. Rev.*, **141**, 4337–4349, https://doi.org/10.1175/MWR-D-12-00350.1.
- Kurihara, Y. M., M. A. Bender, and R. J. Ross, 1993: An initialization scheme of hurricane models by vortex specification. *Mon. Wea. Rev.*, 121, 2030–2045, https://doi.org/10.1175/1520-0493(1993)121<2030:AISOHM>2.0.CO;2.
- Kusaka, H., H. Kondo, Y. Kikegawa, and F. Kimura, 2001: A simple single-layer urban canopy model for atmospheric models: Comparison with multi-layer and slab models. *Bound.-Layer Meteor.*, 101, 329–358, https://doi.org/10.1023/ A:1019207923078.
- Lim, K.-S. S., and S.-Y. Hong, 2010: Development of an effective double moment cloud microphysics scheme with prognostic cloud condensation nuclei (CCN) for weather and climate models. *Mon. Wea. Rev.*, 138, 1587–1612, https://doi.org/ 10.1175/2009MWR2968.1.
- Lorsolo, S., J. L. Schroeder, P. Dodge, and F. D. Marks, 2008: An observational study of hurricane boundary layer small-scale coherent structures. *Mon. Wea. Rev.*, 136, 2871–2893, https://doi.org/10.1175/2008MWR2273.1.
- —, J. A. Zhang, F. D. Marks, and J. Gamache, 2010: Estimation and mapping of hurricane turbulent energy using airborne Doppler measurements. *Mon. Wea. Rev.*, 138, 3656–3670, https://doi.org/10.1175/2010MWR3183.1.
- Louis, J. F., 1979: A parametric model of vertical eddies fluxes in the atmosphere. *Bound.-Layer Meteor.*, **17**, 187–202, https://doi.org/10.1007/BF00117978.
- Marks, F. D., P. G. Black, M. T. Montgomery, and R. W. Burpee, 2008: Structure of the eye and eyewall of Hurricane Hugo (1989). *Mon. Wea. Rev.*, 136, 1237–1259, https://doi.org/ 10.1175/2007MWR2073.1.
- Martilli, A., A. Clappier, and M. Rotach, 2002: An urban surface exchange parameterisation for mesoscale models. *Bound.-Layer Meteor.*, 104, 261–304, https://doi.org/10.1023/A:1016099921195.
- ——, S. Grossman-Clarke, M. Tewari, and K. W. Manning, 2009: Description of the modifications made in WRF.3.1 and short user's manual of BEP. NCAR Tech. Note, 24 pp.
- Masters, F. J., P. J. Vickery, P. Bacon, and E. N. Rappaport, 2010a: Toward objective standardized intensity estimates from surface wind speed observations. *Bull. Amer. Meteor. Soc.*, 91, 1665–1682, https://doi.org/10.1175/2010BAMS2942.1.
- ——, H. W. Tieleman, and J. A. Balderrama, 2010b: Surface wind measurements in three Gulf Coast hurricanes of 2005. J. Wind Eng. Aerodyn., 98, 533–547, https://doi.org/10.1016/ j.jweia.2010.04.003.

- Mellor, G. L., and T. Yamada, 1982: Development of a turbulence closure model for geophysical fluid problems. *Rev. Geophys. Space Phys.*, **20**, 851–875, https://doi.org/10.1029/RG020i004p00851.
- Miller, C., J.-A. Balderrama, and F. Masters, 2015: Aspects of observed gust factors in landfalling tropical cyclones: Gust components, terrain, and upstream fetch effects. *Bound-Layer Meteor.*, 155, 129–155, https://doi.org/10.1007/s10546-014-9989-0.
- Ming, J., J. A. Zhang, R. F. Rogers, F. D. Marks, Y. Wang, and N. Cai, 2014: Multiplatform observations of boundary layer structure in the outer rainbands of landfalling typhoons. *J. Geophys. Res.* Atmos., 119, 7799–7814, https://doi.org/10.1002/2014JD021637.
- Morrison, I., S. Businger, F. Marks, P. Dodge, and J. A. Businger, 2005: An observational case for the prevalence of roll vortices in the hurricane boundary layer. *J. Atmos. Sci.*, 62, 2662–2673, https://doi.org/10.1175/JAS3508.1.
- Nolan, D. S., 2005: Instabilities in hurricane-like boundary layers. *Dyn. Atmos. Oceans*, **40**, 209–236, https://doi.org/10.1016/j.dynatmoce.2005.03.002.
- —, J. A. Zhang, and D. P. Stern, 2009a: Evaluation of planetary boundary layer parameterizations in tropical cyclones by comparison of in situ observations and high-resolution simulations of Hurricane Isabel (2003). Part I: Initialization, maximum winds, and the outer-core boundary layer. *Mon. Wea. Rev.*, 137, 3651–3674, https://doi.org/10.1175/2009MWR2785.1.
- —, D. P. Stern, and J. A. Zhang, 2009b: Evaluation of planetary boundary layer parameterizations in tropical cyclones by comparison of in situ observations and high-resolution simulations of Hurricane Isabel (2003). Part II: Inner-core boundary layer and eyewall structure. *Mon. Wea. Rev.*, 137, 3675–3698, https://doi.org/10.1175/2009MWR2786.1.
- ——, B. D. McNoldy, and J. Y. Ge, 2021a: Evaluation of the surface wind field over land in WRF simulations of Hurricane Wilma (2005). Part I: Model initialization and simulation validation. *Mon. Wea. Rev.*, **149**, 679–695, https://doi.org/10.1175/MWR-D-20-0199.1.
- —, and —, 2021b: Evaluation of the surface wind field over land in WRF simulations of Hurricane Wilma (2005). Part II: Surface winds, inflow angles, and boundary layer profiles. *Mon. Wea. Rev.*, **149**, 697–713, https://doi.org/10.1175/ MWR-D-20-0201.1.
- Pollard, R. T., P. B. Rhines, and R. O. R. Y. Thompson, 1972: The deepening of the wind-mixed layer. *Geophys. Fluid Dyn.*, 3, 381–404.
- Powell, M. D., 1993: Wind measurement and archival under the automated surface observing system (ASOS): User concerns and opportunity for improvement. *Bull. Amer. Meteor. Soc.*, **74**, 615–624, https://doi.org/10.1175/1520-0477(1993)074<0615:WMAAUT>2.0.CO;2.
- —, P. P. Dodge, and M. L. Black, 1991: The landfall of Hurricane Hugo in the Carolinas: Surface wind distribution. *Wea. Forecasting*, **6**, 379–399, https://doi.org/10.1175/1520-0434(1991)006<0379:TLOHHI>2.0.CO;2.
- —, S. H. Houston, and T. A. Reinhold, 1996: Hurricane Andrew's landfall in south Florida. Part I: Standardizing measurements for documentation of surface wind fields. Wea. Forecasting, 11, 304–328, https://doi.org/10.1175/ 1520-0434(1996)011<0304:HALISF>2.0.CO;2.
- Rappaport, E. N., 1994: Hurricane Andrew. *Weather*, **49**, 51–61, https://doi.org/10.1002/j.1477-8696.1994.tb05974.x.
- Raupach, M. R., R. A. Antonia, and S. Rajagoplan, 1991: Roughwall turbulent boundary layers. *Appl. Mech. Rev.*, **44**, 1–25, https://doi.org/10.1115/1.3119492.

- Rotunno, R., and G. H. Bryan, 2012: Effects of parameterized diffusion on simulated hurricanes. *J. Atmos. Sci.*, **69**, 2284–2299, https://doi.org/10.1175/JAS-D-11-0204.1.
- Salamanca, F., A. Krpo, A. Martilli, and A. Clappier, 2010: A new building energy model coupled with an urban canopy parameterization for urban climate simulations. Part I. Formulation, verification, and sensitivity analysis of the model. *Theor. Appl. Climatol.*, 99, 331–344, https://doi.org/10.1007/s00704-009-0142-9.
- ——, A. Martilli, M. Tewari, and F. Chen, 2011: A study of the urban boundary layer using different urban parameterizations and high-resolution urban canopy parameters in WRF. J. Appl. Meteor. Climatol., 50, 1107–1128, https:// doi.org/10.1175/2010JAMC2538.1.
- Shapiro, L. J., 1983: The asymmetric boundary layer flow under a translating hurricane. J. Atmos. Sci., 40, 1984–1998, https:// doi.org/10.1175/1520-0469(1983)040<1984:TABLFU>2.0.CO;2.
- Skamarock, W. C., 2004: Evaluating mesoscale NWP models using kinetic energy spectra. *Mon. Wea. Rev.*, 132, 3019–3032, https://doi.org/10.1175/MWR2830.1.
- —, J. B. Klemp, J. Dudhia, D. O. Gill, D. M. Barker, W. Wang, and J. G. Powers, 2005: A description of the Advanced Research WRF version 2. NCAR Tech. Note NCAR/TN-468+STR, 88 pp., https://doi.org/10.5065/D6DZ069T
- Smith, R. K., 1968: The surface boundary layer of a hurricane. *Tellus*, **20**, 473–484, https://doi.org/10.3402/tellusa.v20i3.10026.
- ——, 2003: A simple model of the hurricane boundary layer. *Quart. J. Roy. Meteor. Soc.*, **129**, 1007–1027, https://doi.org/10.1256/qi.01.197.
- —, and M. T. Mongtomery, 2010: Hurricane boundary-layer theory. *Quart. J. Roy. Meteor. Soc.*, **136**, 1665–1670, https://doi.org/10.1002/qj.679.
- —, and M. T. Montgomery, 2014a: On the existence of the logarithmic surface layer in the inner-core of hurricanes. *Quart. J. Roy. Meteor. Soc.*, **140**, 72–81, https://doi.org/10.1002/qj.2121.
- —, and M. T. Mongtomery, 2014b: Sensitivity of tropical cyclone models to the surface drag coefficient in different boundarylayer schemes. *Quart. J. Roy. Meteor. Soc.*, **140**, 792–804, https://doi.org/10.1002/qj.2057.
- Tewari, M., and Coauthors, 2004: Implementation and verification of the unified NOAH land surface model in the WRF model. 20th Conf. on Weather Analysis and Forecasting/16th Conf. on Numerical Weather Prediction, Seattle, WA, Amer. Meteor. Soc., 14.2a, https://ams.confex.com/ams/pdfpapers/69061.pdf.
- Tiedtke, M., 1989: A comprehensive mass flux scheme for cumulus parameterization in large-scale models. *Mon. Wea. Rev.*, **117**, 1779–1800, https://doi.org/10.1175/1520-0493(1989)117<1779: ACMFSF>2.0.CO;2.
- Uhlhorn, E. W., and D. S. Nolan, 2012: Observational undersampling in tropical cyclones and implications for estimated intensity. *Mon. Wea. Rev.*, 140, 825–840, https://doi.org/ 10.1175/MWR-D-11-00073.1.
- Williams, G. J., R. K. Taft, B. D. McNoldy, and W. H. Schubert, 2013: Shock-like structures in the tropical cyclone boundary

- layer. J. Adv. Model. Earth Syst., 5, 338–353, https://doi.org/10.1002/jame.20028.
- Willoughby, H. E., and P. G. Black, 1996: Hurricane Andrew in Florida: Dynamics of a disaster. *Bull. Amer. Meteor. Soc.*, **77**, 543–549, https://doi.org/10.1175/1520-0477(1996)077<0543: HAIFDO>2.0.CO;2.
- Wu, L., Q. Liu, and Y. Li, 2018: Prevalence of tornado-scale vortices in the tropical cyclone eyewall. *Proc. Natl. Acad. Sci. USA*, 115, 8307–8310, https://doi.org/10.1073/pnas.1807217115.
- Wurman, J., and J. Winslow, 1998: Intense sub-kilometer boundary layer rolls in Hurricane Fran. Science, 280, 555–557, https:// doi.org/10.1126/science.280.5363.555.
- —, and K. Kosiba, 2018: The role of small-scale vortices in enhancing surface winds and damage in Hurricane Harvey (2017). *Mon. Wea. Rev.*, **146**, 713–722, https://doi.org/10.1175/MWR-D-17-0327.1.
- Zhang, C., Y. Wang, and K. Hamilton, 2011: Improved representation of boundary layer clouds over the southeast Pacific in ARW-WRF using a modified Tiedtke cumulus parameterization scheme. *Mon. Wea. Rev.*, 139, 3489–3513, https://doi.org/10.1175/MWR-D-10-05091.1.
- Zhang, F., Y. Weng, J. A. Sippel, Z. Meng, and C. H. Bishop, 2009: Cloud-resolving hurricane initialization and prediction through assimilation of Doppler radar observations with an ensemble Kalman filter. *Mon. Wea. Rev.*, **137**, 2105–2125, https://doi.org/10.1175/2009MWR2645.1.
- Zhang, J. A., and W. M. Drennan, 2012: An observational study of vertical eddy diffusivity in the hurricane boundary layer. *J. Atmos. Sci.*, 69, 3223–3236, https://doi.org/10.1175/JAS-D-11-0348.1.
- ——, and E. W. Uhlhorn, 2012: Hurricane sea surface inflow angle and an observation-based parametric model. *Mon. Wea. Rev.*, 140, 3587–3605, https://doi.org/10.1175/MWR-D-11-00339.1.
- —, K. B. Katsaros, P. G. Black, S. Lehner, J. R. French, and W. M. Drennan, 2008: Effects of roll vortices on turbulent fluxes in the hurricane boundary layer. *Bound.-Layer Meteor.*, 128, 173–189, https://doi.org/10.1007/s10546-008-9281-2.
- —, R. F. Rogers, D. S. Nolan, and F. D. Marks, 2011: On the characteristic height scales of the hurricane boundary layer. *Mon. Wea. Rev.*, 139, 2523–2535, https://doi.org/10.1175/MWR-D-10-05017.1.
- —, —, P. Reasor, E. Ulhlhorn, and F. D. Marks, 2013: Asymmetric hurricane boundary layer structure from drop-sonde composites in relation to the environmental vertical wind shear. *Mon. Wea. Rev.*, **141**, 3968–3984, https://doi.org/10.1175/MWR-D-12-00335.1.
- —, D. S. Nolan, R. F. Rogers, and V. Tallapragada, 2015: Evaluating the impact of improvements in the boundary layer parameterizations on hurricane intensity and structure forecasts in HWRF. *Mon. Wea. Rev.*, **143**, 3136–3155, https:// doi.org/10.1175/MWR-D-14-00339.1.
- Zhu, P., 2008: Impact of land-surface roughness on surface winds during hurricane landfall. *Quart. J. Roy. Meteor. Soc.*, **134**, 1051–1057, https://doi.org/10.1002/qj.265.